Integrated compensatory network is activated in the absence of NCC phosphorylation

P. Richard Grimm, *University of Maryland*
Yoskaly Lazo-Fernandez, *Emory University*
Eric Delpire, *Vanderbilt University*
Susan Wall, *Emory University*
Susan G. Dorsey, *University of Maryland*
Edward J. Weinman, *University of Maryland*
Richard Coleman, *University of Maryland*
James B. Wade, *University of Maryland*
Paul A. Welling, *University of Maryland*

Journal Title: Journal of Clinical Investigation

Volume: Volume 125, Number 5

Publisher: American Society for Clinical Investigation | 2015-05-01, Pages 2136-2150

Type of Work: Article | Final Publisher PDF

Publisher DOI: 10.1172/JCI78558

Permanent URL: https://pid.emory.edu/ark:/25593/rxhq2

Final published version: http://dx.doi.org/10.1172/JCI78558

Integrated compensatory network is activated in the absence of NCC phosphorylation

P. Richard Grimm,[1] Yoskaly Lazo-Fernandez,[2] Eric Delpire,[3] Susan M. Wall,[2,4] Susan G. Dorsey,[5,6] Edward J. Weinman,[1] Richard Coleman,[1] James B. Wade,[1] and Paul A. Welling[1]

[1]Department of Physiology, University of Maryland School of Medicine, Baltimore, Maryland, USA. [2]Department of Medicine, Emory University School of Medicine, Atlanta, Georgia, USA. [3]Department of Anesthesiology, Vanderbilt School of Medicine, Nashville, Tennessee, USA. [4]Department of Physiology, Emory University School of Medicine, Atlanta, Georgia, USA. [5]School of Nursing, University of Maryland, Baltimore, Maryland, USA. [6]Program in Neuroscience, University of Maryland School of Medicine, Baltimore, Maryland, USA.

Thiazide diuretics are used to treat hypertension; however, compensatory processes in the kidney can limit antihypertensive responses to this class of drugs. Here, we evaluated compensatory pathways in SPAK kinase–deficient mice, which are unable to activate the thiazide-sensitive sodium chloride cotransporter NCC (encoded by *Slc12a3*). Global transcriptional profiling, combined with biochemical, cell biological, and physiological phenotyping, identified the gene expression signature of the response and revealed how it establishes an adaptive physiology. Salt reabsorption pathways were created by the coordinate induction of a multigene transport system, involving solute carriers (encoded by *Slc26a4*, *Slc4a8*, and *Slc4a9*), carbonic anhydrase isoforms, and V-type H^+-ATPase subunits in pendrin-positive intercalated cells (PP-ICs) and ENaC subunits in principal cells (PCs). A distal nephron remodeling process and induction of jagged 1/NOTCH signaling, which expands the cortical connecting tubule with PCs and replaces acid-secreting α-ICs with PP-ICs, were partly responsible for the compensation. Salt reabsorption was also activated by induction of an α-ketoglutarate (α-KG) paracrine signaling system. Coordinate regulation of a multigene α-KG synthesis and transport pathway resulted in α-KG secretion into pro-urine, as the α-KG–activated GPCR (*Oxgr1*) increased on the PP-IC apical surface, allowing paracrine delivery of α-KG to stimulate salt transport. Identification of the integrated compensatory NaCl reabsorption mechanisms provides insight into thiazide diuretic efficacy.

Introduction

The sodium chloride cotransporter (NCC) of the *SLC12A3* gene (1, 2) is the principal determinant of NaCl reabsorption in the distal convoluted tubule (DCT) (3) and the key target of thiazide diuretics (4, 5). Recent human genetic and epidemiological studies highlight the importance of NCC in electrolyte balance, blood pressure control, and treatment of hypertension. Indeed, loss-of-function mutations in NCC cause Gitelman syndrome (Online Mendelian Inheritance in Man [OMIM] entry no. 263800), a recessive disorder of urinary salt wasting, variable degrees of hypotension, and a constellation of secondary electrolyte abnormalities including hypokalemia, metabolic alkalosis, hypocalcuria, and hypomagnesemia (6). Genome sequencing efforts in the Framingham cohort revealed that rare loss-of-function mutations in NCC also contribute to blood pressure variation in the general population and reduce hypertension susceptibility (7). As exemplified by the Antihypertensive and Lipid-Lowering treatment to prevent Heart Attack Trial (ALLHAT), the human genetics of NCC have an important therapeutic corollary. This landmark trial demonstrated remarkable benefits of thiazides in the treatment of essential hypertension (8), establishing NCC as a key target of the most cost-effective and medically beneficial antihypertensive agents.

Significant individual differences in the therapeutic response to thiazides are observed, however (9). Moreover, genetic loss of NCC function in humans (6, 10) and mice (3, 11, 12) causes a relatively mild salt-wasting phenotype, especially considering the significant contribution the thiazide-sensitive NCC makes to overall renal NaCl absorption. These observations suggest that strong but variable compensatory mechanisms blunt the blood pressure response and prevent deleterious changes in fluid and electrolyte balance when NCC is compromised. The nature of this compensation is poorly understood. In NCC KO mice, activation of pendrin-mediated chloride absorption (13), ENaC (11, 14), and NHE3-mediated sodium reabsorption (14) have been shown to contribute, but an integrated molecular understanding of adaptive responses to NCC inhibition has been wanting. To develop a better appreciation of the response, we sought to identify the gene networks in the kidney that are activated to drive NaCl reabsorption when NCC phosphorylation is compromised, as occurs in the absence of the STE20/SPS-1–related proline-alanine–rich protein kinase (15, 16).

A serine/threonine kinase–signaling cascade involving SPAK and the with-no-lysine kinases WNK1 and WNK4 has recently emerged as a key pathway for maintaining and activating NCC on demand (17). This signaling cascade is stimulated by intravascular volume depletion or dietary sodium restriction through angiotensin II (18–21) and/or aldosterone (22–24) and adrenergic

▶ Related Commentary: p. 1793

Conflict of interest: The authors have declared that no conflict of interest exists.
Submitted: August 14, 2014; **Accepted:** February 9, 2015.
Reference information: *J Clin Invest*. 2015;125(5):2136–2150. doi:10.1172/JCI78558.

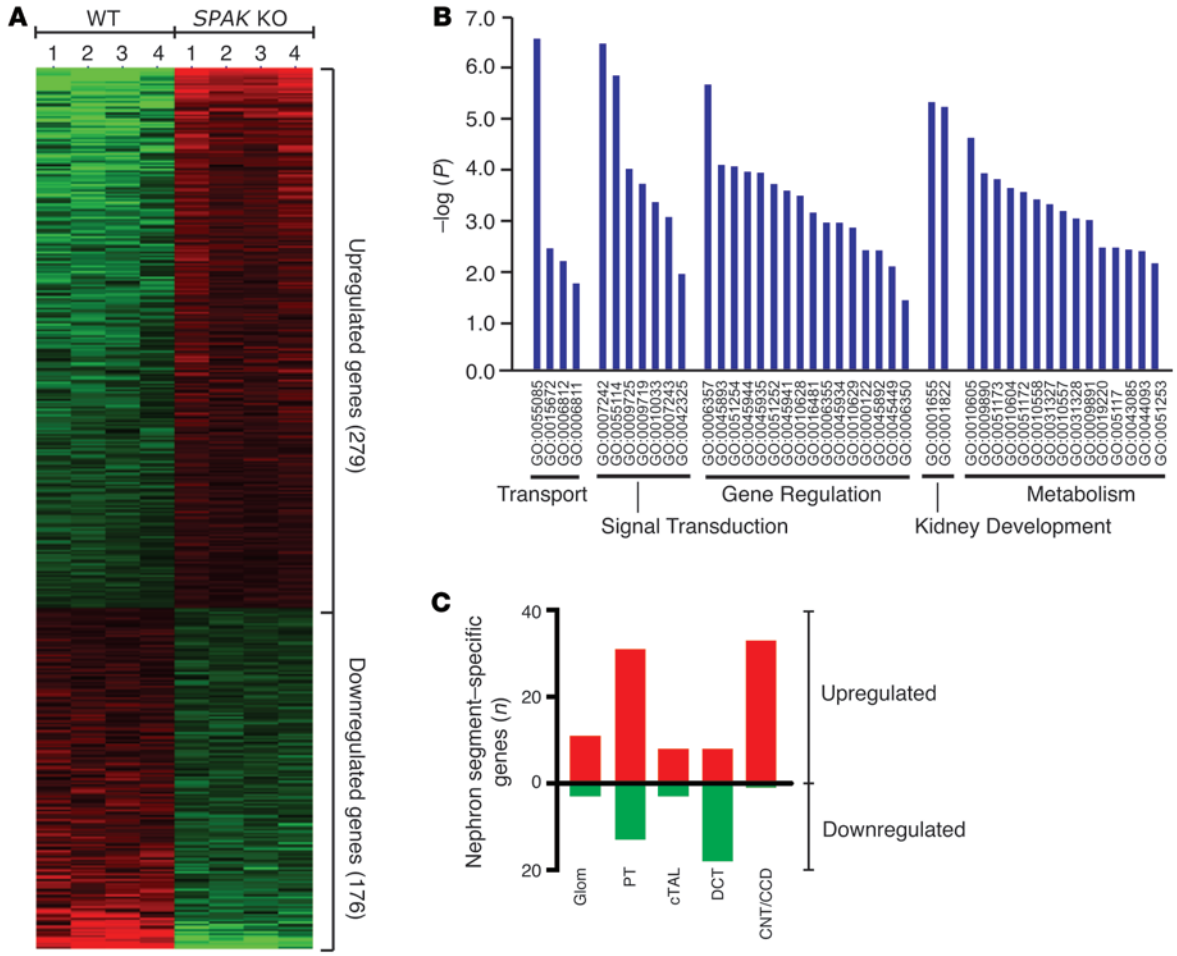

Figure 1. *SPAK* KO transcript profile. (**A**) Heatmap rendering of the transcript expression profile of *SPAK* KO and WT mice (n = 4 mice per group). Differentially expressed genes in kidney cortex are shown. Each individual block represents the relative transcript level of an individual gene. Genes are arranged by row according to the FDR (from high [top] to low [bottom], with a lower-limit FDR <0.05). Each column represents the profile of an individual mouse. (**B**) GO classification of genes by biological function revealed that the *SPAK* KO profile was significantly enriched in 5 major functional classes. Level of significance (–log of the *P* value) is plotted for each significant GO term. Individual GO terms are arranged according to major functional class. (**C**) Number of *SPAK*-upregulated (red) and -downregulated (green) profile genes that were exclusively expressed in individual nephron segments. Glom, glomerulus; cTAL, cortical TAL.

factors (25, 26). Once stimulated, WNK kinases bind to and phosphorylate SPAK (27). Phosphorylated SPAK can then interact with and directly phosphoactivate NCC, making it the key terminal kinase in the cascade (27). In familial hyperkalemic hypertension (aka PHAII; OMIM 145260), mutations in *WNK1* and *WNK4* (28) aberrantly activate the signaling pathway, causing hyperphosphorylation of SPAK and NCC (29), hypertrophy of the DCT (30), excessive urinary sodium retention, and hypertension. Likewise, a common variant in *SPAK*, which has gain-of-function properties, has been identified as a hypertension-susceptibility allele (31).

A prevailing function of SPAK is to activate NCC via phosphorylation (32–34). The full-length, active form of SPAK predominantly colocalizes with NCC within the DCT apical membrane (31). Moreover, *SPAK* KO mice display a phenotype that is identical to that of NCC-deficient mice and humans with Gitelman syndrome (32–34). While SPAK can potentially phosphoregulate the loop diuretic–sensitive sodium-potassium-chloride cotransporter NKCC2 in the thick ascending limb (TAL), NKCC2 becomes hyperphosphorylated in *SPAK* KO mice (32–34). Activation of NKCC2 has been suggested to play a major role in the maintenance of salt balance in *SPAK* KO mice, but the glomerular-tubular feedback system, which would reduce glomerular filtration rate (GFR), may blunt these effects. Compensatory salt reabsorption is more likely to have major effects at segments distal to the macula densa. Because the salt-losing phenotypes of Gitelman syndrome, *SPAK* KO mice, and NCC KO mice are similar and relatively mild compared with the predicted effects of loss of NCC function, we hypothesized that multiple common compensatory mechanisms blunt natriuresis and chloriuresis and protect against a major drop in blood pressure.

The present study was designed to identify and characterize the gene networks and physiological pathways that underpin the compensatory response. Our results identify renal salt transport and signaling systems that are induced to maintain salt balance and blood pressure in the absence of NCC phosphorylation.

Results

To identify genes that are regulated to maintain salt balance when phosphorylation of NCC is compromised, genome-wide analysis of

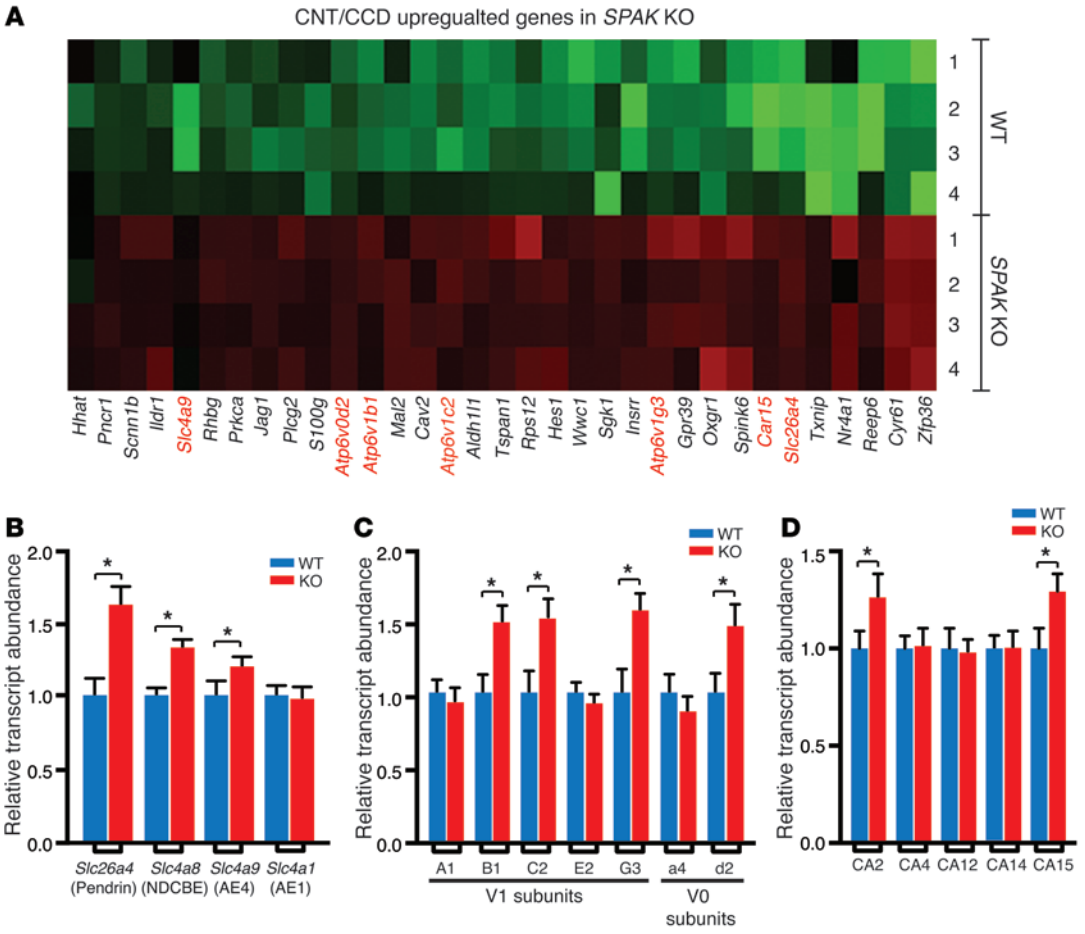

Figure 2. CNT/CCD transcript profile reveals induction of an IC transport pathway in *SPAK* KO mice. (**A**) Heatmap of CNT/CCD-specific genes that are upregulated in *SPAK* KO mice. More than one-third of the upregulated genes were expressed in PP-ICs (highlighted in red), and the majority of these are involved in ion transport. qPCR survey of IC transcripts, including SLC-type transporter family members (**B**), V-ATPase subunits (**C**), and carbonic anhydrase (CA) genes (**D**), confirmed the results of microarray and identified several other IC genes as being differentially expressed in *SPAK* KO mice. Data represent the mean ± SEM. n = 6 animals per genotype. *$P < 0.05$ by 2-tailed t test for WT versus KO.

transcript levels was performed on kidney cortex samples from WT and *SPAK* KO mice using the Affymetrix whole-genome GeneChip Mouse Gene 1.0 ST Array, which represents all mouse genes and contains more than 28,000 total transcripts. A distinct profile of 279 upregulated and 176 downregulated transcripts was identified in the *SPAK* KO mice (n = 4 WT versus n = 4 KO) using standard statistical analyses and expression levels as filtering thresholds (FDR <0.05 and relative transcript changes ± 120%) (Figure 1A). All identified genes that were selected for further analysis (n = 53 genes, see below) were verified as regulated transcripts by quantitative PCR (qPCR), providing strong support for the analytical approach. Gene ontological (GO) analysis (Figure 1B) using the Database for Annotation, Visualization and Integrated Discovery (DAVID) (35) indicated that the *SPAK* KO array was especially enriched in molecules that function in transport, signal transduction, gene regulation, kidney development, and metabolism.

To understand how these genes might be coregulated into functional networks, nephron segment–specific transcript profiles were created by selecting profile genes that normally have a highly restricted pattern of expression along the nephron (36) and then sorting them into groups according to their sites of expression (see Methods). Ninety-one of the upregulated genes and 32 of the downregulated genes could be classified in this way. As shown in Figure 1C, proximal tubule (PT) and connecting tubule/cortical collecting duct (CNT/CCD) transcript profiles were enriched in upregulated genes. By contrast, the DCT profile was enriched in downregulated genes (e.g., *SPAK*, parvalbumin, *Slc12a3*, *Trpm6*, and *Cnnm2*), consistent with the atrophy of this segment that is observed when NCC activity is inhibited or lost (11, 33, 34, 37, 38).

Activation of the electroneutral NaCl reabsorption transporter network. A salient feature of the CNT/CCD transcript profile is the presence of transport genes that have been implicated in mediating NaCl reabsorption by β- and non-α/non-β intercalated cells (ICs) (Figure 2A). Because both β- and non-α/non-β ICs express the Cl/HCO_3 exchanger pendrin (39–41), we refer to them collectively herein as pendrin-positive ICs (PP-ICs) for simplicity. In addition to verifying the transcript abundance increase of pendrin (*Slc264a4*), which is activated in NCC KO mice (13, 42), the profile revealed an increase in AE4 (*Slc4a9*), numerous V-type proton ATPase subunits (V0 subunit d2 and the V1 subunits B1, C2, and G3), and 2 different isoforms of carbonic anhydrase (CA2 and CA15). A comprehensive qPCR survey of IC transporters (Fig-

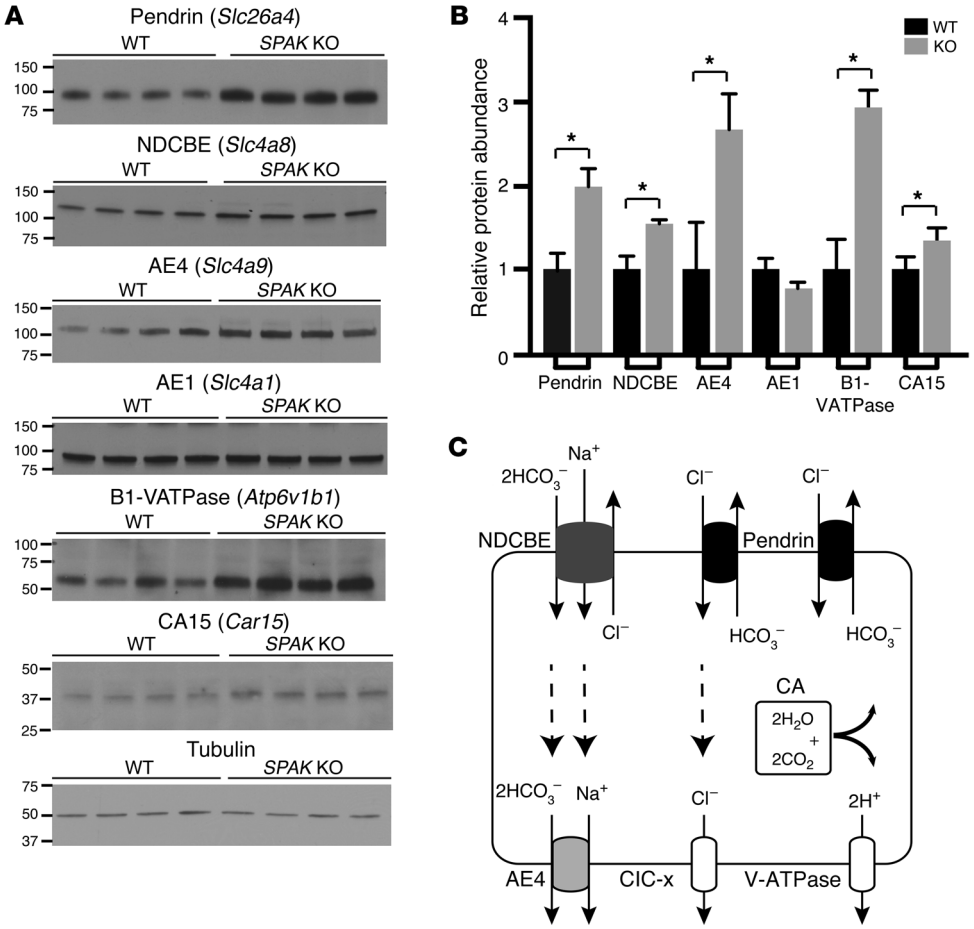

Figure 3. Increased abundance of PP-IC transport proteins in *SPAK* KO mice. (**A**) Western blot and (**B**) summary quantification of pendrin, NDCBE, AE4, AE1, the B1 subunit of V-ATPase, and CA15 in WT versus *SPAK* KO mice. Data represent the mean ± SEM. $n = 4$ animals per group. $^*P < 0.05$ by 2-tailed t test for WT versus KO. (**C**). Each of the upregulated molecules comprise elements of the electroneutral NaCl reabsorption system. Proposed transport model (see Discussion).

ure 2B), as well as proton ATPase subunits (Figure 2C) and carbonic anhydrase genes (Figure 2D), confirmed the array findings and revealed that the sodium-dependent chloride bicarbonate cotransporter NDCBE (*Slc4a8*) (43) was also increased. In striking contrast, the key basolateral Cl^-/HCO_3^- exchanger of the α-IC AE1 (*Slc4a1*) (44, 45) was absent in the *SPAK* KO transcript profile, and no changes in its transcript abundance were detected in the *SPAK* KO kidney by qPCR (Figure 2B).

Further experiments explored the effect of *SPAK* gene ablation on the protein abundance of IC transporters for which antibodies are available. Immunoblot analysis (Figure 3, A and B) confirmed an increased abundance of the PP-IC proteins pendrin, NDCBE, AE4, B1-VATPase, and CA15. As a negative control, no change was detected in the abundance of the α-IC protein AE1.

Collectively, these observations identify a highly organized regulatory response in PP-ICs that orchestrates the simultaneous activation of a multitransporter network. Recent studies provide strong evidence that each of the upregulated transport molecules functions as an integral component of an electroneutral NaCl reabsorption system (Figure 3C and see Discussion). Its activation provides a means to increase NaCl reabsorption and compensate for the loss of NCC function.

Enhanced apical expression of pendrin and chloride reabsorption. Because apical plasma membrane pendrin abundance is strongly regulated through membrane-trafficking processes (46–49), we examined the effect of *SPAK* gene ablation on pendrin localization within β-type PP-ICs. In contrast to the diffuse cytoplasmic and weak apical membrane pendrin labeling that was observed in PP-ICs from WT mice, intense pendrin labeling was observed in the apical regions of PP-ICs from *SPAK* KO mice (Figure 4A). Quantitative measurements of pendrin pixel intensity across the apical membrane and cytoplasm in multiple PP-ICs ($n = 50$ cells per animal, 5 animals per group) (Figure 4B) confirmed that the increase in pendrin abundance at the apical membrane in *SPAK* KO mice was robust and statistically significant (Figure 4C). As assessed by measurements of transepithelial chloride flux in isolated perfused CCDs, the change in pendrin was associated with an increase in tubular transport of chloride (Figure 4D). Indeed, we found that CCDs from *SPAK* KO mice had approximately 6-fold greater chloride reabsorption than did WT CCDs (13.3 ± 4.2 vs. 2.4 ± 1.7 pmol/mm/min; $P < 0.05$, $n = 4$). Thus, augmentation of pendrin abundance and apical localization were paralleled by an expected increase in chloride reabsorption.

Remodeling of the distal nephron. The CNT/CCD profile is also enriched in factors that control nephrogenesis (Figure 1B), and some of these have been implicated in IC differentiation and IC subtype conversion. Accordingly, we considered the possibility that an IC remodeling process is a chief underpinning of PP-IC transporter network activation. To explore this question, IC subtypes were identified with cell markers (PP-IC and α-IC AE1-positive cells) and counted. In addition, ICs were colocalized with nephron segment–specific markers so that potential sites

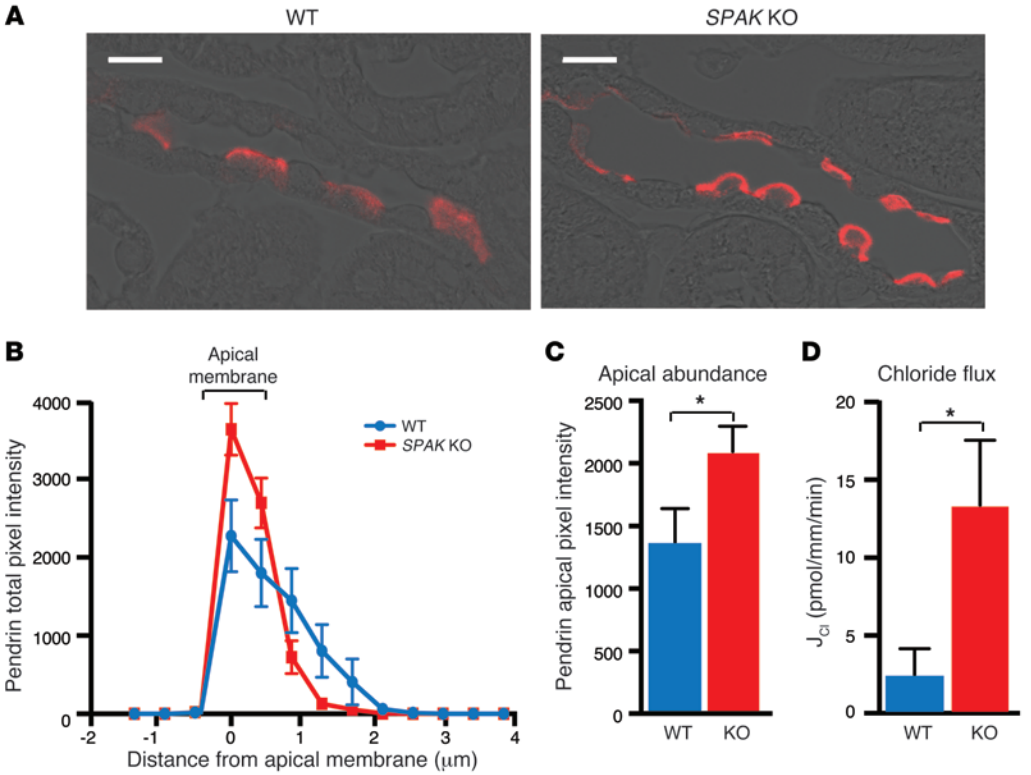

Figure 4. Pendrin translocates to the apical membrane in *SPAK* KO mice. (**A**) Immunolocalization of pendrin (red) in typical CNTs of WT and *SPAK* KO mice. Scale bars: 10 μm. (**B**) Quantitative image analysis of pendrin. Pendrin pixel intensity was measured over a 6-μm distance from the tubule lumen into the cytoplasm at 0.4 μm–increment resolution. The bracketed area delineates the apical membrane. (**C**) Summary data of apical membrane–delimited pendrin abundance. Apical pendrin increased by 55% in *SPAK* KO mice compared with that in WT. Data represent the mean ± SEM. n = 5 animals per genotype with 50 or more cells from each animal. *P > 0.05 by 2-tailed t test for WT versus KO. (**D**) Cl^- absorption (J_{Cl}) was measured in isolated CCDs from WT and *SPAK* KO mice and perfused in vitro. Data represent the mean ± SEM. n = 4 animals per genotype. *P < 0.05 by 2-tailed t test for WT versus KO.

of remodeling could be identified. As shown in Figure 5A, *SPAK* KO mice displayed an obvious and remarkable increase in the number of PP-ICs. This was paralleled by a reciprocal reduction in the number of α-ICs, without remarkable changes in the absolute number of ICs (1.1% increase in total IC numbers in *SPAK* KO mice relative to WT mice). The remodeling response was greatest in the CNT, weaker in the CCD, and not present in the late DCT (Figure 5B). Thus, activation of the PP-IC transporter network can be explained, at least in part, by a cellular remodeling process that replaces α-ICs with PP-ICs in the CNT and CCD. The response was most predominant in the CNT.

This IC remodeling process was accompanied by an increase in principal cells (PCs), especially in the CNT (21.5% increase in PC numbers) (Figure 5C). Stereological morphometric measurements of individual distal nephron segments revealed that the increase in PCs is accompanied by an increase in CNT length (Figure 5D), and this precisely offsets the decline in DCT1, which fails to develop or atrophies in *SPAK* KO mice (33, 34) and in other models of NCC dysfunction (11, 37).

We considered that the kidney development genes identified in the profile may contribute to the remodeling process. We focused on profile components that are involved in the NOTCH signaling cascade, because this pathway has been implicated in determining PC/IC fate (50). As identified by transcription profiling and confirmed by qPCR experiments, upregulation of the NOTCH receptor ligand jagged 1 (*Jag1*) and downregulation of *Jag2* were accompanied by an increase in a key NOTCH-activated transcriptional factor, hairy and enhancer of split 1 (*Hes1*), as well as iroquois homeobox molecules (*Irx1* and *Irx2*) (Figure 6A). The signature is indicative of activation of NOTCH signaling in the adult *SPAK* KO mouse kidney cortex. Western blot analyses confirmed that HES1 and JAG1 protein abundance was increased in the *SPAK* KO mouse (Figure 6, B and C).

Further experiments were performed to determine where NOTCH signaling occurs. As observed by immunofluorescence confocal microscopy, nuclear localization of HES1, a reporter of NOTCH activation, was predominantly observed in nuclei of cells within the CNT (Figure 6D). Colabeling of HES1 with PC (AQP2) and IC markers revealed that HES1 was exclusively induced within PC nuclei (Figure 6E and see below). JAG1 labeling was also increased along the CNT, and immunodetectable signal was observed within both PCs and ICs, but it was not possible with IHC to distinguish between cells that expressed the full-length receptor on the cell surface and those that had JAG bound to NOTCH. Nevertheless, these observations suggest that JAG1 activates NOTCH signaling in PCs.

Together, these observations suggest that activation of the NOTCH signaling pathway in CNT PCs coordinates a program of PC differentiation and proliferation, allowing the CNT to replace the dystrophic DCT1. The expansion of the CNT and the increase

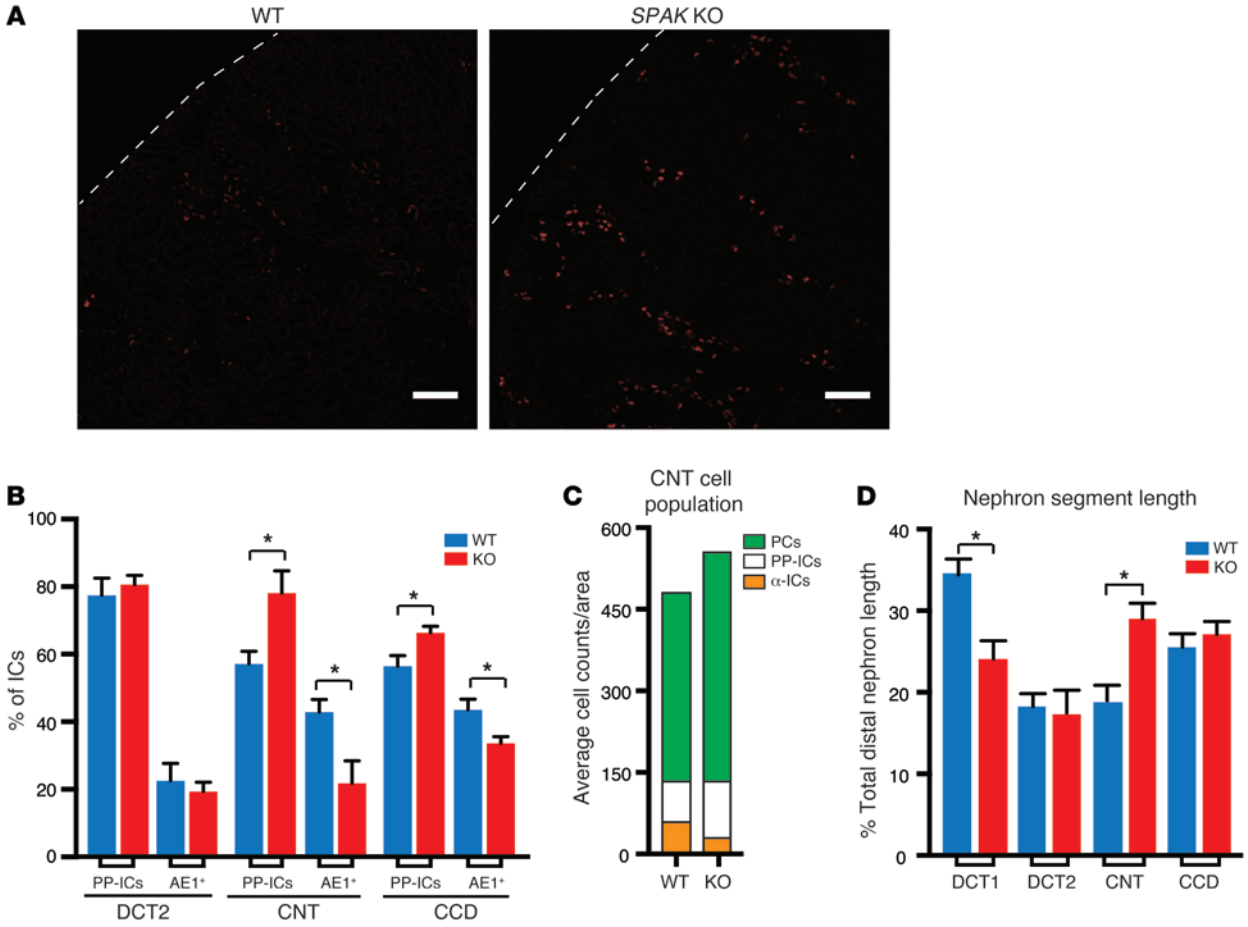

Figure 5. Cellular remodeling process replaces α-ICs with PP-ICs and expands CNT with PCs in *SPAK* KO mice. (**A**) Immunolocalization of PP-ICs (pendrin, red) in the kidney cortex of WT and *SPAK* KO mice. Scale bars: 100 μm. (**B**) Relative number of IC subtypes (β- and non-α/non-β ICs [PP-ICs] and α-ICs [AE1$^+$]) in the late DCT (DCT2), CNT, and CCD. For these studies, calbindin and AQP2 were used to identify nephron segments (calbindin alone = DCT2; calbindin plus AQP2 = CNT; AQP2 alone = CCD). Data represent the mean ± SEM. n = 4 animals per group. *$P < 0.05$ by 2-tailed t test for WT versus KO. (**C**) Quantitative summary of CNT cell subtype counts (numbers of PCs, α-ICs, and PP-ICs per unit area are plotted in the stacked diagram). (**D**) Morphometric length measurements of DCT1, DCT2, CNT, and CCD in WT and *SPAK* KO mice. Data represent the mean ± SEM. n = 5 animals per genotype. *$P < 0.05$ by 2-tailed t test for WT versus KO. (DCT, identified by the presence of parvalbumin and NCC; DCT2, identified as calbindin- and NCC-positive tubules; CNT, identified as calbindin- and AQP2-positive tubules; and CCD, identified as calbindin-negative, AQP2-positive tubules).

in PCs augment the capacity for electrogenic NaCl reabsorption via the epithelial sodium channel ENaC.

Na^+ absorption in PCs is determined by ENaC (25, 51), and the *SPAK* KO transcript profile as well as qPCR identified the ENaC β and γ subunits as upregulated genes (Figure 7A). The serum glucocorticoid–induced kinase SGK1, which increases ENaC apical abundance (52, 53), and claudin 4, a determinant of a Cl^--selective paracellular pathway in the distal nephron (54), were also identified as increased on the array. Taken together, the transcript profile provides support for the idea that ENaC-mediated sodium reabsorption is activated in parallel with a paracellular Cl^- reabsorption pathway and a transcellular electroneutral NaCl transport system in PP-ICs.

To test ENaC function, we assessed the diuretic and natriuretic responses to benzamil, which is considered to be a specific ENaC inhibitor at the low dose used here (1.0 mg/kg). *SPAK* KO mice exhibited significantly increased responses to benzamil compared with that in WT mice, verifying that a functional increase in ENaC-mediated sodium reabsorption accompanies PC expansion (Figure 7, B and C). Together with the increase in PP-ICs and activation of electroneutral salt reabsorption, the cellular remodeling response provides two powerful mechanisms to offset the loss of NCC activity.

Paracrine activation of NaCl reabsorption in PP-ICs by α-ketoglutarate. One mechanism to activate pendrin is revealed by the identification of *Oxgr1* as an upregulated gene in the CNT/CCD transcript profile. *Oxgr1* encodes a novel GPCR for α-ketoglutarate (α-KG) (55), and recent studies demonstrated that this receptor is responsible for activating pendrin-dependent chloride reabsorption (56). As shown in Figure 8A, qPCR confirmed *Oxgr1* as an upregulated transcript in *SPAK* KO mice. As assessed by immunoblot analysis with specific OXGR1 antibodies (Supplemental Figure 1; supplemental material available online with this article; doi:10.1172/JCI78558DS1), the increase in *Oxgr1* transcripts was paralleled by an increase in protein abundance. OXGR1 protein migrates at the predicted size (38 kDa) and in higher molecular weight forms (~75 and 100 kDa), consistent with glycosyla-

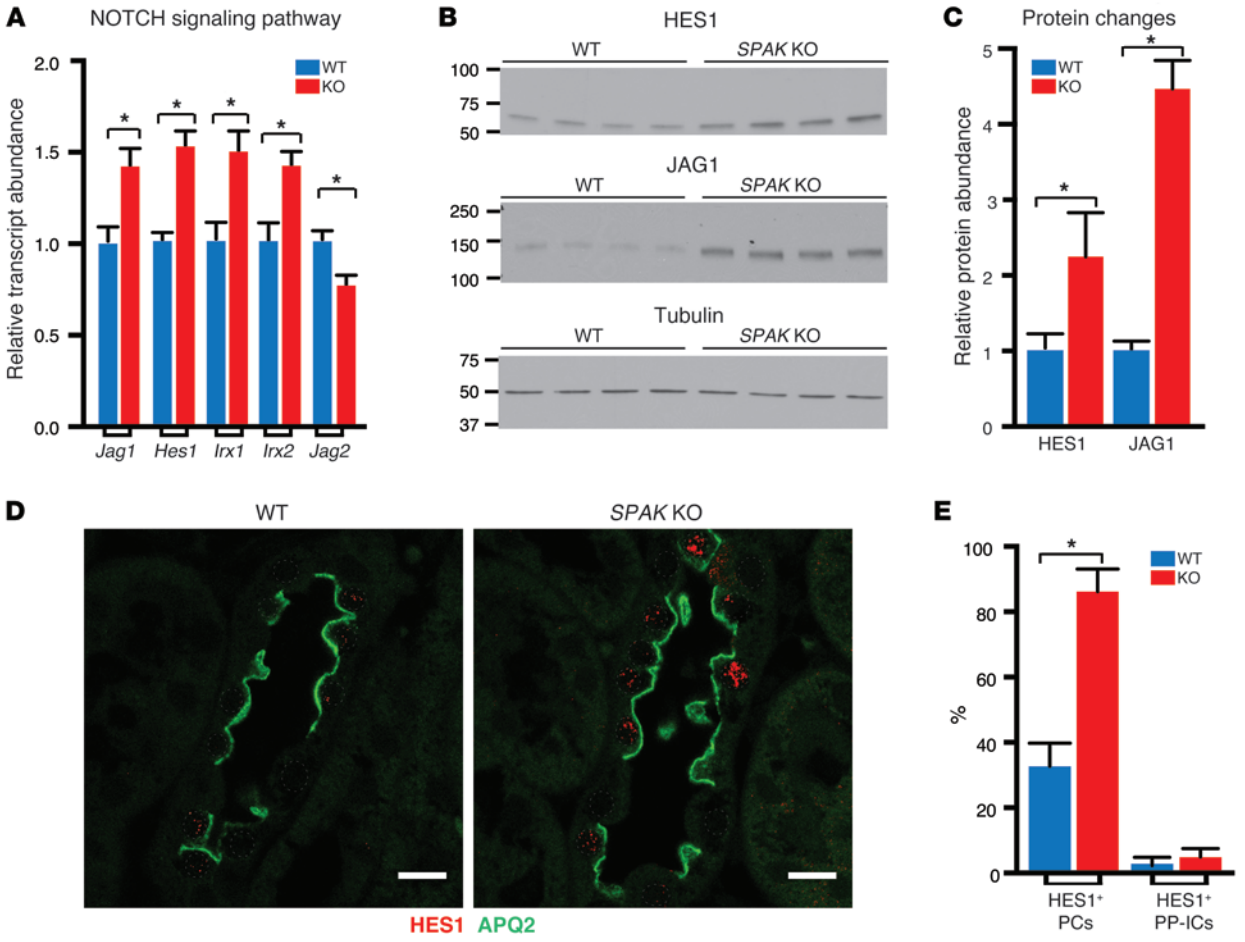

Figure 6. NOTCH signaling is induced in *SPAK* KO mice. (**A**) qPCR of NOTCH signaling molecules identified in the *SPAK* KO profile as upregulated (*Jag1*, *Hes1*, *Irx1*, *Irx2*) or downregulated genes (*Jag2*). Data represent the mean ± SEM. $n = 6$ animals. *$P < 0.05$ by 2-tailed t test for WT versus KO. (**B**) Western blot analysis of the NOTCH effector molecule HES1 and the NOTCH ligand JAG1 and (**C**) quantitative summary of relative HES and JAG1 protein abundance. Data represent the mean ± SEM. $n = 4$ animals. *$P < 0.05$ by 2-tailed t test for WT versus KO. (**D**) Immunolocalization of HES1 in WT and *SPAK* KO CNT (HES1, red; AQP2-labeled PCs, green; CNTs identified as calbindin$^+$ tubules, not shown. Scale bars: 10 μm. Note: HES1 was almost exclusively expressed in PC nuclei. (**E**) Quantitative summary of HES1$^+$ PCs and PP-ICs in the CNT (percentage of total subtype). Data represent the mean ± SEM. $n = 4$ animals per genotype. *$P < 0.05$ by 2-tailed t test for WT versus KO.

tion and/or receptor oligomerization (Figure 8B); all forms were increased in *SPAK* KO mice relative to WT mice (Figure 8C). Immunofluorescence confocal microscopy revealed that OXGR1 was exclusively expressed in PP-ICs at the apical membrane and was more abundant in *SPAK* KO mice than in WT mice (Figure 8, D and E). Thus, OXGR1 is poised to hyperactivate pendrin, so long as there is sufficient α-KG in the pro-urine.

The PT transcript profile revealed a mechanism to enhance the release of α-KG into the tubular fluid for paracrine delivery to OXGR1 (Figures 9 and 10). In addition to its key role as an intermediate of the Krebs (TCA) cycle, α-KG is also produced in the PT as an intermediate of ammoniagenesis, a process that is stimulated by acidosis or potassium depletion through the activation of glutamine and glutamate deamination enzymes and uptake transporters (57–59). Remarkably, the SPAK KO PT profile (Figure 9A) contained many of the key transporters (NaDC1, OAT10, SAT2, SNA3) and enzymes (glutamate oxaloacetate transaminase) that facilitate ammoniagenesis and could potentially enhance α-KG production. The observation prompted a comprehensive qPCR survey of the ammoniagenesis pathway and measurements of urinary ammonium and α-KG excretion.

Two of the four known sodium-dependent glutamine uptake proteins (60), the apically localized SAT2 (*Slc38a2*) and the basolateral SNAT3 (*Slc38a3*) (61), were identified as upregulated genes in the array and verified by qPCR (Figure 9B). Additional qPCR screening identified increased levels of the apically expressed sodium-dependent glutamine transporter B^{0}AT1 (*Slc6a19*) (62) and the basolateral glutamate transporter AGT1 (*Slc7a13*) (63), but not ASCT2 (*Slc1a5*), in the SPAK KO kidney.

Genes encoding the dicarboxylate transporter (64) *Slc13a2* (NaDC1) and organic anion exchangers (*Slc22a13*, OAT10; ref. 65) were also identified as upregulated on the array (Figure 9A) and verified using qPCR (Figure 9C), along with *Slc13a3* (NaDC3) and the sodium-hydrogen exchanger NHE3 (*Slc9a3*). By contrast, the α-KG transporter OAT1 (*Slc22a6*), which mediates α-KG efflux across the basolateral membrane (66, 67) and would limit α-KG secretion, was found on the downregulated transcript profile and verified by qPCR. The transport properties of these transporters

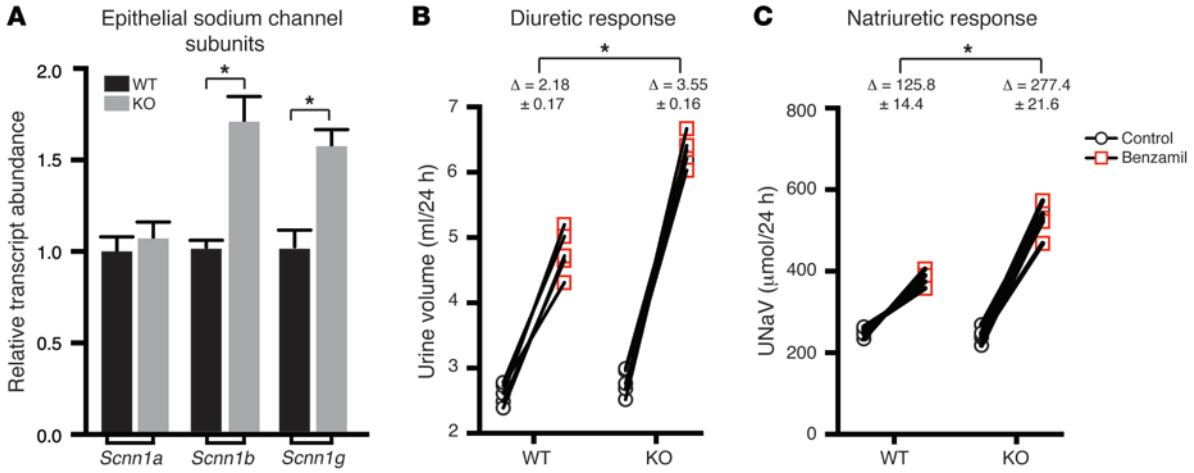

Figure 7. ENaC expression and function are enhanced in *SPAK* KO mice. (**A**) β-ENaC was identified in the *SPAK* KO profile as an upregulated gene. qPCR screening of all ENaC subunits verified the upregulation of the β subunit but also identified the γ subunit as upregulated in *SPAK* KO mice. Data represent the mean ± SEM. $n = 6$ animals. *$P < 0.05$ by 2-tailed t test for WT versus KO. The 24-hour diuretic (**B**) and natriuretic (**C**) responses of WT and *SPAK* KO mice to a single dose (1.0 μg/mg) of benzamil showed that basal urine volumes and UNaV were not different between the 2 animal groups. Additionally, both groups had demonstrated a significant increase in urine and sodium excretion when treated with benzamil. However, the change in urine and sodium excretion was significantly higher in *SPAK* KO mice than that in WT mice, suggesting increased ENaC-dependent sodium reabsorption in *SPAK* KO mice. Data represent the mean ± SEM. $n = 5$ animals. *$P < 0.05$ by 2-tailed t test, comparing the change in diuretic (**B**) and the change in natriuretic response (**C**) in WT versus KO mice.

predict that their regulation would increase α-KG and ammonia secretion (see Figure 9D).

Glutaminase (GLS) and glutamate dehydrogenase (GLUD1), the key regulated enzymes that deaminate glutamine and glutamate to produce ammonia and α-KG (Figure 10A), were also detected as upregulated transcripts by qPCR (Figure 10B). By contrast, enzymes that drive the reverse reactions to produce glutamine from α-KG were downregulated. Phosphoenolpyruvate carboxykinase (*PEPCK* of the *PCK1* gene), which is activated for ammoniagenesis in states of acidosis to convert excess α-KG into glucose and generate bicarbonate (68, 69), was not on the SPAK transcript profile, and no change in transcript abundance could be detected by qPCR. These data indicate that the PT is poised to enhance the production of α-KG.

Plasma and urine α-KG were evaluated to test whether such a mechanism results in increased α-KG in the tubular fluid. As shown in Figure 10, C and D, urine α-KG levels normalized by urinary creatinine increased nearly 3-fold in *SPAK* KO mice, with no detectable change in the plasma concentration, consistent with increased secretion of α-KG into the tubular fluid. The response was matched by an increase in urinary ammonia excretion (Figure 10E), consistent with the predicted parallel activation of ammoniagenesis and α-KG secretion. A slight alkalization of the urine (Figure 10F) was also observed, consistent with parallel activation of pendrin-mediated bicarbonate secretion.

Taken together, the data identify a paracrine signaling system that connects PT ammoniagenesis and α-KG production and secretion to the activation of pendrin-mediated salt transport in the distal nephron.

Discussion

Our data unveil a multifaceted and integrated compensatory mechanism that preserves salt balance when the activity of the thiazide-sensitive NaCl cotransporter NCC is compromised, as occurs in the absence of the SPAK kinase. We found that a distal nephron remodeling process and the activation of a paracrine signaling system act together to induce salt-reabsorbing transport pathways in the CNT and CCD.

Induction of the PP-IC transport network. The compensatory response highlights PP-ICs, which have recently emerged as an important avenue of regulated salt transport in the kidney (70, 71). Extending the recent discovery that increased expression of pendrin is critical for maintaining salt reabsorption in NCC KO mice (13), our observations reveal that the induction of pendrin is part of a highly organized regulatory response involving the simultaneous activation of a multitransporter network. On the basis of physiological studies in different transporter KO mice, Eladari and coworkers proposed that each of the upregulated transport molecules, identified here, acts as an integral component of an electroneutral NaCl reabsorption machine in PP-ICs (Figure 3C and ref. 71). According to their model, the concerted activity of pendrin-mediated Cl/HCO_3 exchange and NDCBE-mediated $Na/HCO_3/Cl$ exchange at the apical membrane allows the uptake of sodium and chloride from the pro-urine (43, 72), while the activity of the H^+-ATPase, the AE4 Na/HCO_3 cotransporter (71), and an undefined Cl^- channel facilitate NaCl efflux across the basolateral membrane into the interstitium. In this scheme, the H^+-ATPase powers the system, creating a favorable outwardly directed HCO_3^- gradient for the bicarbonate-dependent transporters pendrin and AE4 to drive electroneutral salt reabsorption (73). It is not presently clear what driving forces are available for NDCBE to mediate sodium uptake (70), but it seems likely that enhanced sodium delivery in the absence of NCC provides a sufficient chemical gradient to drive inward sodium movement across the apical membrane and increase sodium reabsorption in parallel with pendrin-dependent chloride uptake. Our observation that the entire

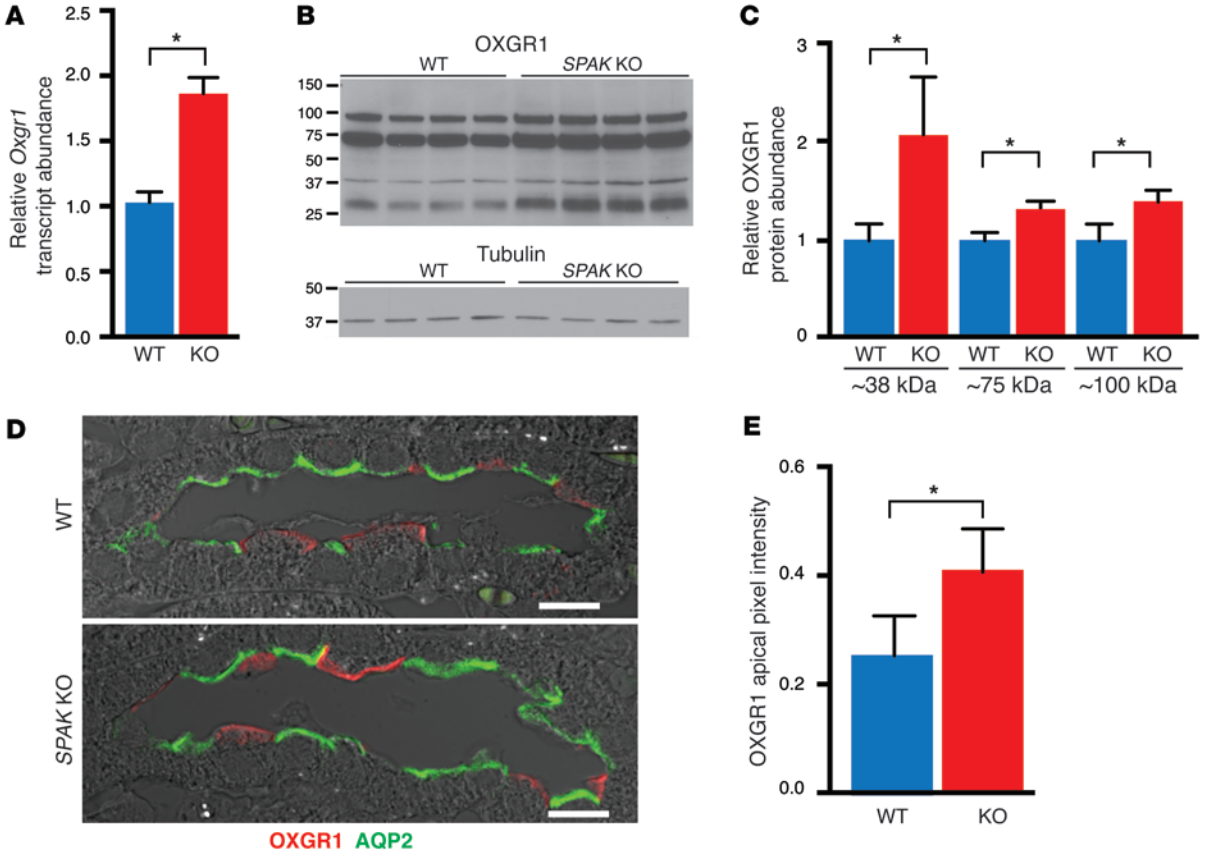

Figure 8. Induction of the α-KG–activated GPCR OXGR1 in *SPAK* KO mice. (**A**) qPCR of *Oxgr1* transcript summary data. Data represent the mean ± SEM. $n = 5$ animals per group. *$P < 0.05$ by 2-tailed t test for WT versus KO. (**B**) Western blot of OXGR1. (**C**) Quantitative summary of relative protein abundance. Data represent the mean ± SEM. $n = 4$ animals. *$P < 0.05$ by 2-tailed t test for WT versus KO. (**D**) Confocal images of OXGR1 (red) in representative CNTs from WT and *SPAK* KO mice. Scale bars: 10 μm. Note the increased expression of OXGR1 at the IC apical membrane in *SPAK* KO mice compared with that in WT mice. Cell types were identified by the presence of AQP2 (PCs, green), AE1 (α-IC marker, not shown), and PNA (PP-ICs, not shown). (**E**) Quantification of OXGR1 apical membrane abundance. Data represent the mean ± SEM. 50 cells per animal; $n = 5$ animals per group. *$P < 0.05$ by 2-tailed t-test for WT versus KO.

transport system behaves as a coregulated unit offers further support for the NaCl-reabsorbing transport model.

Activation of the PP-IC transport system not only provides a means to limit urinary salt loss, but it can also compensate for the hypochloremic metabolic alkalosis that can develop with loss of NCC function. Although the precise stoichiometry of transporters in the PP-IC transport system is unknown, current evidence suggests that it allows PP-ICs to secrete bicarbonate in exchange for the reabsorption of NaCl. Indeed, pendrin/NCC double-KO mice develop much more severe metabolic alkalosis and salt wasting than do mice lacking NCC or pendrin alone (13). Likewise, thiazide diuretic treatment was reported to cause severe hypochloremic metabolic alkalosis and salt wasting in a child with pendrin syndrome (74).

Distal tubule remodeling. Activation of the PP-IC transporter pathway is explained in part by a remarkable distal nephron cellular remodeling process involving an increase in the number of PP-ICs. Because the response is matched by a decrease in α-ICs, it is tempting to speculate that IC remodeling is driven by the differentiation of α-ICs into PP-ICs, but further studies will be required to explore this idea and test other possible mechanisms. Convincing in vitro and in vivo data indicate that acidosis provokes the differentiation of α-ICs from β-ICs (75) in a process involving the induction of the cell adhesion factor hensin (76) and β1 integrin (77). Nevertheless, neither hensin nor β1 integrin was identified as a downregulated gene in the *SPAK* KO mouse profile, and it is not clear whether the IC conversion works in the opposite direction. In fact, PP-ICs have been reported to be progenitors of α-ICs and PCs in vitro (78), and, as far as we know, the differentiation of α-ICs into PP-ICs is unprecedented. It is also conceivable that the remodeling is shaped by differences in IC proliferation rates, as has been observed in response to loop diuretics and high dietary salt intake (79), although this does not profoundly alter the ratio of the different IC types in the manner observed here in our *SPAK* KO mice. During the early postnatal period, PP-ICs appear to arise from undifferentiated precursor cells (80), raising another possibility that the neonatal differentiation process is recapitulated and exaggerated in the adult kidney when NCC-mediated transport is inhibited and the DCT atrophies. The profile of nephrogeneic factors identified here should provide a roadmap for future studies to elucidate the basis of the IC remodeling mechanism.

In fact, our identification and characterization of NOTCH signaling elements revealed that embryonic nephrogenic cell fate determinants can be reactivated in the adult kidney to shape the distal nephron remodeling process. In the developing collecting

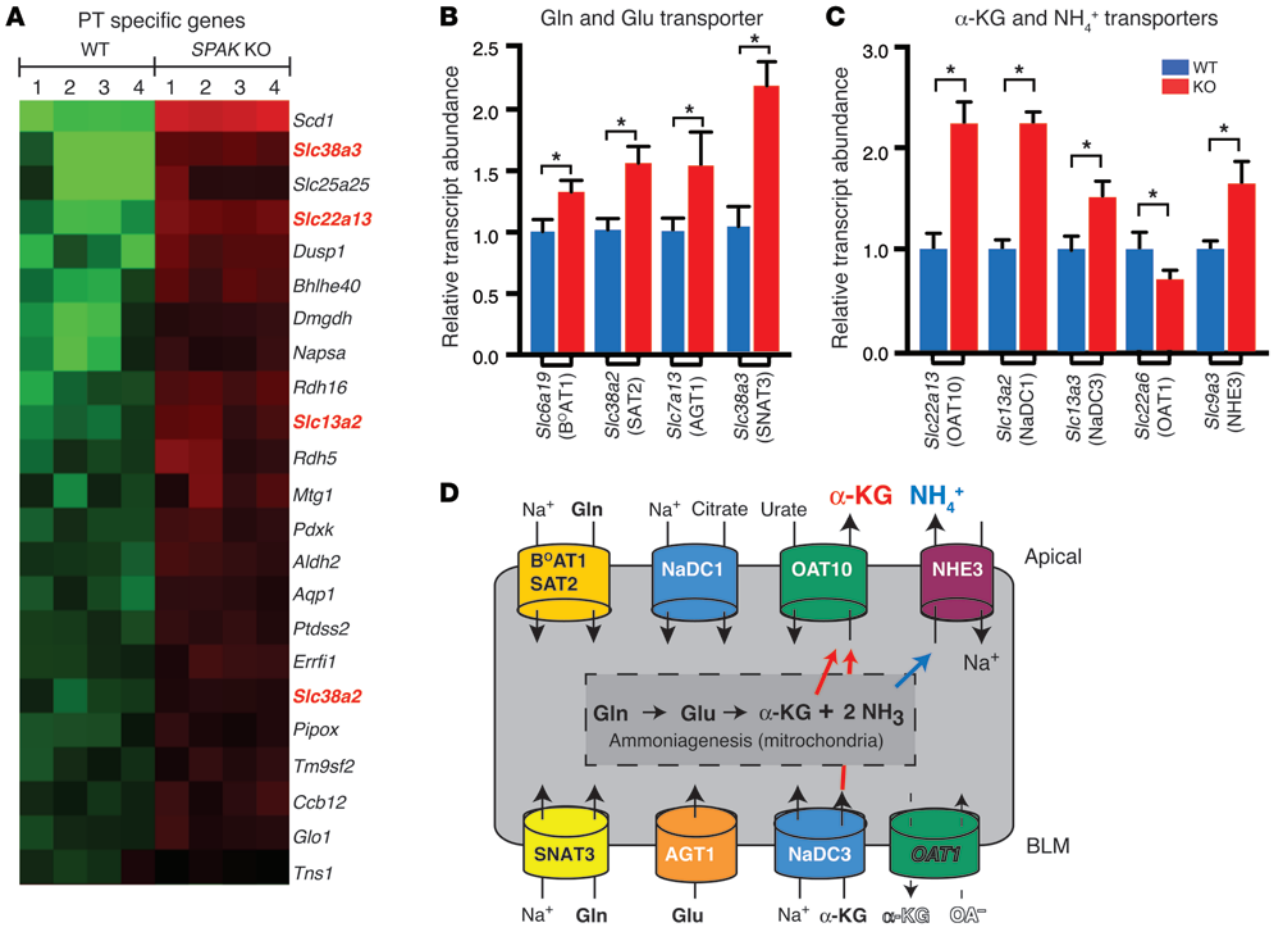

Figure 9. Induction of PT transport proteins in *SPAK* KO mice facilitates α-KG production and secretion. (**A**) PT-specific gene profile revealed upregulation of 2 glutamine (Gln) transporters (*Slc38a3* and *Slc38a2*) and 2 α-KG transporters (*Slc22a13* and *Slc13a2*). (**B** and **C**) Summary of qPCR screen for glutamine and glutamate transporters, α-KG transporters, and *Nhe3*. Data represent the mean ± SEM. $n = 6$ animals per group. $^*P < 0.05$ by 2-tailed *t* test for WT versus KO. (**D**) Transport model showing that stimulation of Gln and Glu uptake transporters provides a substrate for ammoniagenesis and α-KG production, while the differential regulation of α-KG transporters favors α-KG delivery into the tubular fluid for paracrine activation of OXGR1. BLM, basolateral membrane.

duct, NOTCH signaling is required to drive the differentiation of PCs (50). Our observations that NOTCH signaling was selectively activated in PCs of adult *SPAK* KO mice, concurrent with their proliferation, strongly suggest that this developmental process is recapitulated in the adult kidney to increase the number of PCs and expand the CNT. It will be interesting to learn the lineage of these NOTCH-activated PCs. Upon recovery from lithium-induced nephrogenic diabetes insipidus (81) or potassium deficiency (82), PCs have been reported to arise from the conversion of α-ICs, raising the possibility that NOTCH signaling in the *SPAK* KO mouse drives a similar process to expand PCs at the expense of α-ICs. Given that the morphological changes in the distal nephron of the *SPAK* KO mouse are remarkably similar to those in the NCC KO mouse (11), in which the CNT is also expanded to replace an atrophic distal tubule, it seems likely that NOTCH signaling provides a common mechanism to drive PC differentiation and proliferation when sodium reabsorption in the early distal tubule is compromised.

The collective distal nephron remodeling process ultimately allows pendrin- and ENaC-mediated transport processes to be efficiently coordinated. In recent years, it has become appreciated that the activities of ENaC and pendrin are often coupled together. For example, genetic ablation of pendrin causes a reduction in ENaC (83), and activation of pendrin stimulates ENaC by increasing luminal bicarbonate and alkalizing the tubular fluid (84). Other positive coupling mechanisms involving pendrin-dependent ATP release from PP-ICs and purinergic activation of ENaC have been reported (85, 86). By increasing the number of PP-ICs and PCs together, the distal nephron remodeling process is poised to amplify pendrin-ENaC coupling so as to activate the electrogenic and electroneutral salt transport pathways in parallel and optimally enhance NaCl reabsorption in distal nephrons.

α-KG/OXGR1 paracrine signaling. Our data reveal that salt reabsorption through the PP-IC pathway is also activated by induction of a newly discovered intrarenal α-KG paracrine signaling system. Remarkably, increased expression of OXGR1, the α-KG GPCR on the PP-IC apical membrane, is accompanied by an increase in α-KG within the tubular fluid. By simultaneously activating both of the key elements of the pathway, the paracrine system is poised to provide a powerful means to augment PP-IC salt transport in the absence of NCC function. Other pendrin activators, especially

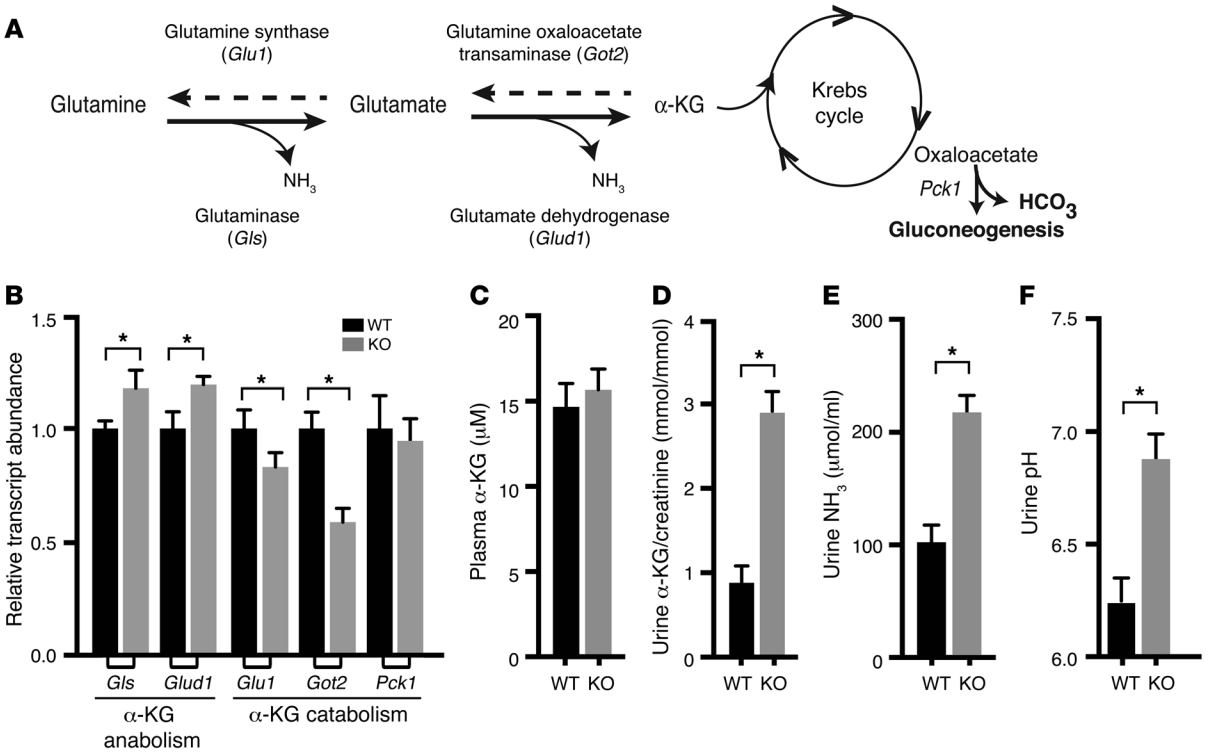

Figure 10. Upregulation of key enzymes necessary for ammoniagenesis and α-KG production activate α-KG secretion. (**A**) Reversible multienzyme ammoniagenesis pathway produces α-KG from glutamine. (**B**) Summary of qPCR survey of key enzymes responsible for α-KG anabolism (*Gls* and *Glud1*) and catabolism (*Glu1* and *Got2*). Data represent the mean ± SEM. $n = 6$ animals. $^*P < 0.05$ by 2-tailed t test for WT versus KO. Summary data for plasma α-KG (**C**), as well as for urinary excretion of α-KG (**D**) and ammonia (NH_3 and NH_4^+) (**E**) and urine pH (**F**). Data represent the mean ± SEM. $n = 6$ animals. $^*P < 0.05$ by 2-tailed t test for WT versus KO.

aldosterone, angiotensin II, and alkalosis (46, 47), can be elevated in Gitelman syndrome, as well as in NCC- and *SPAK* KO mice, and likely work with α-KG to maximize pendrin-mediated transport.

We found that enhanced production of α-KG results from induction of the multigene ammoniagenesis pathway. The concerted upregulation of glutamine and glutamate uptake transporters (SAT2 [*Slc38a2*], SNAT3 [*Slc38a3*], B^0AT1 [*Slc6a19*], and AGT1 [*Slc7a13*]), the upregulation of glutamine and glutamate deaminating enzymes (*Gls* and *Glud1*), and the downregulation of α-KG catabolic enzymes (*Glu1* and *Got2*) cause the production of ammonia to increase in the *SPAK* KO mouse, similar to the response that is provoked by acidosis and potassium deficiency. But unlike acidosis, which also activates phosphoenolpyruvate carboxykinase (PEPCK) to consume α-KG and generate glucose and bicarbonate (69, 87), PEPCK is not induced in *SPAK* KO mice, and, as a result, α-KG levels increase rather than diminish.

Differential regulation of PT α-KG transporters explains how enhanced α-KG production is accompanied by an increase in α-KG delivery to the tubular fluid. Net α-KG uptake from the blood across the basolateral membrane is predicted to increase from the upregulation of NaDC3 (64, 88), which uses the inwardly directed electrochemical sodium gradient to transport α-KG into the cell across the basolateral membrane, and from the downregulation of OAT1, which mediates basolateral α-KG efflux (66, 89). The transporter(s) responsible for carrying α-KG across the apical membrane into the tubular fluid have not been established, but our identification of *Oat10* as an upregulated gene provides a clue. Because OAT10 is expressed on the PT apical membrane and has the capacity to exchange organic anions for the efflux of short-chain fatty acids (65), we propose that its activation leads to an increased efflux of α-KG across the apical membrane.

Although further studies will be required to identify the factors responsible for activating the paracrine signaling process, there is reason to suspect that hypokalemia and metabolic alkalosis are involved. Both can develop as a consequence of NCC inhibition, and each have the capacity to either stimulate α-KG production or enhance α-KG secretion. Dietary alkaline loading, by itself, has recently been shown to enhance urinary α-KG excretion (56). Because alkalosis usually suppresses ammoniagenesis, it is more likely to activate the secretory transport of α-KG than to stimulate production. Differential regulation of NaDC3 and the OAT transporters observed here may offer an explanation. By contrast, potassium deficiency induces ammoniagenesis (59, 90) and therefore probably activates the production of α-KG. By stimulating α-KG through separate pathways, the combined effects of potassium deficiency and alkalosis are expected to have potentiating effects on the stimulation of α-KG as a paracrine factor.

Such a system would be ideally suited to limit hypokalemic metabolic alkalosis. Ammonium excretion has been proposed to be stimulated in states of potassium deficiency as an adaptive mechanism to reduce urinary potassium loss (59, 91). If accompanied by an increase in α-KG signaling, activation of bicarbonate

secretion by pendrin will limit the renal acid excretion that otherwise accompanies the increase in ammonium secretion and help compensate for the metabolic alkalosis.

Hormones that stimulate ammoniagenesis or enhance the expression of α-KG transporters should also be considered as candidate activators of the paracrine pathway. Observations that angiotensin II stimulates ammoniagenesis (92), for example, raise the intriguing possibility that it also activates α-KG signaling. Parallel activation of ammonium (acid) secretion and pendrin-mediated Cl/HCO_3 exchange would have the net effect of stimulating chloride reabsorption without disrupting the acid-base balance. Such a system may be especially important in states of intravascular volume depletion when pendrin is activated to restore sodium balance and blood pressure.

Summary. In summary, gene profiling, combined with biochemical, cell biological, and physiological phenotyping, defined adaptive mechanisms that maintain salt balance in the absence of SPAK and NCC phosphorylation. It will be of interest to understand whether overactivation of these adaptive pathways contributes to the development of diuretic resistance.

Methods

Animals. The generation and phenotypic characterization of *SPAK* KO (*SPAK*$^{-/-}$) mice have been described in detail previously (33, 34, 93). Heterozygous pairs, backcrossed more than 20 generations, were bred to generate WT and KO mice for experimentation. Male pups (~4 weeks of age) were screened by PCR genotyping of tail DNA to identify the KO allele. Because a PCR-based strategy cannot distinguish heterozygous and KO animals, the final determination of genotype was assessed using SPAK antibodies in Western blot analyses of kidney lysates. For these studies, mice were fed a control diet (1% K^+, 0.32% Na^+, 0.9% Cl^-) (TD.88238; Teklad Lab Animal Diets, Harlan Laboratories) after weaning. Paired 8-week-old WT and KO littermates were compared. Mice were maintained on a 12-hour light/12-hour dark cycle, with lights on at 6 a.m. Food and water were available ad libitum. *SPAK* KO animals used for these studies had the same phenotypic properties as those previously reported (see Supplemental Table 1).

Sample collection, preparation, and analysis. Animals were anesthetized by i.p. injection with ketamine/xylazine (100 mg/kg ketamine, 10 mg/kg xylazine), and the left kidney was removed, dissected into cortex and medulla samples, and stored in RNAlater (QIAGEN) or flash-frozen in liquid nitrogen for later RNA and protein extraction. Blood samples were collected from the carotid artery and immediately spun down for measurements of plasma α-KG, creatinine, and electrolytes. Urine samples were collected from the anesthetized mice by puncturing the bladder with a 24-gauge needle and drawing out urine with a syringe. Plasma and urine creatinine levels were measured using the QuantiChrom Creatinine Assay Kit (BioAssay Systems) according to the manufacturer's protocol. Plasma and urine α-KG levels were assayed using a Colorimetric Assay (BioVision). Measured urinary α-KG concentration was normalized to urine creatinine to ensure that changes were the result of changes in absolute excretion rather than the result of urine concentration/dilution. Urinary NH_3/NH_4 was measured using the Ammonia Reagent Set (Pointe Scientific Inc.).

RNA isolation, microarray, qPCR. RNA was extracted and purified from the cortex of 4 *SPAK* KO and 4 WT littermate mice using TRIzol reagent (Life Technologies). A microarray assay was performed using the Affymetrix GeneChip (Mouse Gene 1.0 ST), containing probes for more than 28,000 transcripts, and analyzed on an Affymetrix GeneChip 3000 system (Biopolymer-Genomics Core Facility at the University of Maryland School of Medicine). Quality control analysis, robust multiarray average (RMA) normalization, and linear model for microarray-based (LIMMA-based) differential expression analysis were subsequently performed. Array data were deposited in the NCBI's Gene Expression Ominbus (GEO GSE60728) (94). qPCR was used to verify the altered expression of array-identified candidate genes and to assess differential gene expression of proteins involved in the compensatory response, using a Roche LightCycler 480 qPCR system and LightCycler 480 SYBER Green I Master reagents pathways. All reactions were performed in triplicate for each animal (n = 6 WT and n = 6 KO). Relative transcript abundance was calculated using the Pfaffl equation (95), a derivation of the ΔΔCt method. Unlike the latter, the Pfaffl equation accounts for actual efficiency of doubling within the linear range of amplification, a value that can vary depending on template concentration. The values represented in the figures are normalized Pfaffl values relative to WT.

Enrichment analysis of array genes. The DAVID database was used to sort array-identified genes by biological function and then statistically rank the most overrepresented (enriched) functional categories (35).

Nephron segment–specific transcript profiles. Serial analysis of gene expression (SAGE) data (36) from isolated mouse nephron segments was used as a reference to identify profile genes that are specifically expressed within individual nephron segments. Segment-specific genes were defined as genes that have at least 75% of their total transcript count within a single nephron segment. Profile genes that matched this criterion where sorted into groups, according to their sites of expression, to generate nephron segment–specific transcript profiles.

Sample preparation for Western blot analysis. Mouse cortex tissue was sonicated in HEENG buffer (20 mM Hepes [pH 7.6], 125 mM NaCl, 1 mM EDTA, 1 mM EGTA, 10% glycerol) containing 1% Triton and 0.5% SDS with protease and phosphatase inhibitors. Samples were sonicated for three 10-second pulses. The samples were rotated in 4°C for 1 hour at low speed (10 *g*) and then spun down at high speed (20 *g*) for 10 minutes to pellet-insoluble material. The supernatant was collected and quantified for protein yield using a bicinchoninic acid protein assay reagent kit (Pierce). Equal amounts of kidney protein were suspended in Laemmli buffer (at room temperature for 45 minutes) and resolved on 4% to 15% gradient SDS-PAGE gels, then transferred to Amersham Hybond ECL membranes (GE Healthcare) and blocked in Tris-buffered saline with 0.1% Tween-20 (TBS-T) containing 5% nonfat dry milk (NFDM) for 1 hour at room temperature. Membranes were then incubated in 5% NFDM containing primary antibody (4°C, overnight), washed in TBS-T, incubated in 5% NFDM containing HRP-conjugated secondary antibody, and then washed 3 times for 10 minutes each time in TBS-T. Bound antibodies were then revealed using an enhanced chemiluminescence reagent (Pierce) and fluorography. Protein quantification was done by scanning autofluorograms, followed by ImageJ analysis (NIH). Bands were measured in the linear range of the fluorographic signal. Duplicate gels were processed and developed in parallel. After detection of the target, membranes were stripped and reprobed for tubulin as a loading control. The full, uncut gels are provided in the supplemental material.

Immunolocalization. Anesthetized mice were fixed by perfusion with 2% paraformaldehyde in PBS via the left ventricle for 5 minutes

at room temperature. The kidneys were then removed and fixed for an additional 24 hours at 4°C in the same fixative, rinsed in PBS, and embedded in paraffin. Cross-sections of 3 μm thickness, cut at the level of the papilla, were picked up on chrome-alum gelatin–coated glass coverslips and dried on a warming plate. The sections were then deparaffinized in 2 xylene baths and 2 absolute ethanol baths (5 minutes for each bath), and rehydrated in a graded ethanol series to distilled water.

For epitope retrieval, the coverslips were placed in a pH 8 aqueous solution of Tris (1 mM), EDTA (0.5 mM), and SDS (0.02%). The retrieval solution was heated to boiling in a microwave oven, transferred to a conventional boiling water bath for 15 minutes, and then allowed to cool to room temperature before the sections were thoroughly washed in distilled water to remove the SDS.

Sections were preincubated for 30 minutes with Image-iT blocking solution (Invitrogen), rinsed in PBS, and then preincubated for an additional 30 minutes in a solution of 2% BSA, 0.2% fish gelatin, 5% normal donkey serum, and 0.2% sodium azide in PBS. Tissues were thoroughly rinsed with TBS to remove the PBS. Incubations with specific antibodies (as described above) diluted in TBS containing 1% BSA, 0.2% fish gelatin, 0.1% Tween-20, 10 mM $CaCl_2$, and 0.2% sodium azide took place overnight in a humid chamber at 4°C. After thorough washing in a high-salt wash (incubation medium plus added NaCl at 0.5 M), Alexa Fluor secondary antibodies (Molecular Probes) were diluted 1:100 in incubation medium and applied to samples for 1 hour, followed by a high-salt wash, and then mounted onto slides with VECTASHIELD Mounting Media (Vector Laboratories).

Antibodies. The following antibodies were used for Western blot analysis and/or immunolocalization studies: mouse anti-calbindin D-28K (IHC 1:600; catalog c-9848; Sigma-Aldrich); chicken anti-AQP2 (from James Wade; IHC 1:100); rabbit anti-pendrin (from Susan Wall; Western blot 1:5,000, IHC 1:50,000); goat anti-pendrin (IHC 1:50; catalog sc-16894; Santa Cruz Biotechnology Inc.); goat anti-NDCBE (Western blot 1:100; catalog sc-169346; Santa Cruz Biotechnology Inc.); goat anti-B1-VATPase (Western blot 1:50; catalog sc-21206; Santa Cruz Biotechnology Inc.); goat anti–CA-XV (Western blot 1:100; catalog sc-54772; Santa Cruz Biotechnology Inc.); rabbit anti-AE4 (Western blot 1:100; catalog AE41-A; Alpha Diagnostic International); rabbit anti-AE1 (Western blot 1:1,000, IHC 1:50; catalog AE11-A; Alpha Diagnostic International); rabbit anti-tubulin (Western blot 1:2,000; catalog 2144s; Cell Signaling Technology); rabbit anti-HES1 (Western blot 1:1,000, IHC 1:3,000; catalog 11988s; Cell Signaling Technology); rabbit anti-OXGR1 (Western blot 1:100, IHC 1:25; catalog PA5-32960; Thermo Scientific); and goat anti-JAG1 (Western blot 1:200, IHC 1:100; catalog sc-6011; Santa Cruz Biotechnology Inc.).

Measurement of transepithelial Cl^- flux in perfused, isolated CCDs. Littermate *SPAK* KO and WT mice were fed the control diet described above and drank water ad libitum. CCDs were dissected from medullary rays and perfused at flow rates of 2 to 3 nl/min in the presence of symmetric, HCO_3^--buffered physiological solutions containing 125 mM NaCl, 24 mM $NaHCO_3$, 2.5 mM K_2HPO_4, 2 mM $CaCl_2$, 1.2 mM $MgSO_4$, and 5.5 mM glucose. Tubules were equilibrated at 37°C for 15 minutes before starting collections. Cl^- concentration was measured in the perfusate and collected samples using a continuous-flow fluorimeter and the Cl^--sensitive fluorophore 6 methoxy-*N*-(3-sulfopropyl) quinolinium (SPQ) (Molecular Probes, Life Technologies), as described previously (96–98). Transepithelial Cl^- flux, J_{Cl}, was calculated according to the following equation: $J_{Cl} = (C_o - C_L)Q/L$, where C_o and C_L are the perfusate and collected fluid Cl^- concentrations, respectively. Q is the flow rate in nl/min, and L is the tubule length. Net fluid transport was taken to be zero, since net fluid flux has not been observed in CCDs when perfused in vitro in the presence of symmetric solutions and in the absence of vasopressin (99, 100). J_{Cl} is expressed in pmol/mm/min.

Quantification of nephron segment length in kidney sections. Low-power images of the kidney cortex were acquired using a Zeiss LSM 510 confocal microscope with a ×10 objective lens and appropriate filters. The DCT1, DCT2, CNT, and CCD could be identified for quantification using antibodies against the segment-specific proteins parvalbumin (parva), calbindin D28 (calbn), and aquaporin 2 (AQP2): DCT1 = $parva^+$ $calbn^-AQP2^-$; DCT2 = $parva^-calbn^+AQP2^-$; CNT = $parva^-calbin^+AQP2^+$; CCD = $parva^-calbn^-AQP2^+$; and 3 fluorophores. Every cortical distal nephron segment in each tissue section was classified using this system.

Total DCT1, DCT2, CNT, and CCD lengths were determined with a curvilinear stereometric system developed by Merz (101) and previously published by our group (33). For these measurements, a curve linear test grid composed of evenly spaced curved lines was superimposed over the images of the cortex. Tubule length, L, was determined by $L = I \times D$, where I is the number of intersections between the curvilinear test grid and the tubule, and D is the distance between corresponding points on either the same line or the adjacent line, which was 21 μm for our text grid. The length of each identifiable DCT1, DCT2, CNT, and CCD was measured and normalized to the area of the cortex in the image. Sections from 5 animals of each genotype were evaluated in this manner, and the figures represent the average of each genotype ($n = 5$).

Quantification of distal nephron cell types in kidney sections. Quantification of pendrin- and AE1-expressing ICs in the DCT2, CNT, and CCD was performed by labeling sections with antibodies against pendrin (goat), AE1 (rabbit), and the segment-specific markers calbindin D28 (mouse) and aquaporin 2 (chicken), as described above. The total number of each cell type (PCs = calbindin $D28^+$ and/or aquaporin 2^+; α-ICs = $AE1^+$; non-α/non-β and β-ICs = $pendrin^+$) in each segment was counted within the entire cortex of 4 WT and 4 *SPAK* KO animals. Similar methods were used to localize and subsequently quantify HES1 expression within the cortical distal nephron.

Quantification of pendrin and OXGR1 intracellular localization in kidney sections. Evaluation of pendrin and OXGR1 intracellular localization was performed by measuring the pixel intensity over a 6-μm distance from the tubule lumen into the cytoplasm at 0.4 μm–increment resolution using Velocity 3D Image Analysis Software (PerkinElmer). Random selection of 50 cells from each of 5 WT and 5 *SPAK* KO mice ($n \geq 250$ cells per group) was performed, and the cells were measured and compared.

Statistics. Data are presented as the mean ± SEM. Statistical analysis was performed using GraphPad Prism, version 6 (GraphPad Software). Statistical significance was determined by a 2-tailed *t* test when comparing 2 groups and by 1-way randomized ANOVA, followed by a Tukey's multiple comparisons test when comparing multiple groups. A *P* value of less than 0.05 was considered significant.

Study approval. The IACUCs of the University of Maryland School of Medicine and Emory University School of Medicine approved all experimental procedures.

Acknowledgments

This work was supported by grants from the NIH (DK63049, DK54231, and DK093501, to P.A. Welling; DK32839, to J.B. Wade;

GM074771 and DK093501, to E. Delpire; P30NR014129, to S.G. Dorsey; DK55881, to E.J. Weinman; 5T32HL072751, to P.R. Grimm; DK46493, to S.M. Wall; and T32DK07656, to Y. Lazo-Fernandez) and the Research Service, Department of Veterans Affairs (to E.J. Weinman).

Address correspondence to: Paul A. Welling, University of Maryland School of Medicine, Department of Physiology, Bressler Research Building 5-029, 655 West Baltimore Street, Baltimore, Maryland 21201, USA. Phone: 410.706.3851; E-mail: pwelling@umaryland.edu.

1. Gamba G. The thiazide-sensitive Na^+-Cl^- cotransporter: molecular biology, functional properties, and regulation by WNKs. *Am J Physiol Renal Physiol*. 2009;297(4):F838–F848.
2. Gamba G, et al. Primary structure and functional expression of a cDNA encoding the thiazide-sensitive, electroneutral sodium-chloride cotransporter. *Proc Natl Acad Sci U S A*. 1993;90(7):2749–2753.
3. Schultheis PJ, et al. Phenotype resembling Gitelman's syndrome in mice lacking the apical Na^+-Cl^- cotransporter of the distal convoluted tubule. *J Biol Chem*. 1998;273(44):29150–29155.
4. Kunau RT Jr, Weller DR, Webb HL. Clarification of the site of action of chlorothiazide in the rat nephron. *J Clin Invest*. 1975;56(2):401–407.
5. Ellison DH, Velazquez H, Wright FS. Thiazide-sensitive sodium chloride cotransport in early distal tubule. *Am J Physiol*. 1987;253(3 pt 2):F546–F554.
6. Simon DB, et al. Gitelman's variant of Bartter's syndrome, inherited hypokalaemic alkalosis, is caused by mutations in the thiazide-sensitive Na-Cl cotransporter. *Nat Genet*. 1996;12(1):24–30.
7. Ji W, et al. Rare independent mutations in renal salt handling genes contribute to blood pressure variation. *Nat Genet*. 2008;40(5):592–599.
8. Furberg CD, et al. Major outcomes in high-risk hypertensive patients randomized to angiotensin-converting enzyme inhibitor or calcium channel blocker vs diuretic: The Antihypertensive and Lipid-Lowering Treatment to Prevent Heart Attack Trial (ALLHAT). *JAMA*. 2002;288(23):2981–2997.
9. Turner ST, et al. Genomic association analysis of common variants influencing antihypertensive response to hydrochlorothiazide. *Hypertension*. 2013;62(2):391–397.
10. Riveira-Munoz E, et al. Gitelman's syndrome: towards genotype-phenotype correlations? *Pediatr Nephrol*. 2007;22(3):326–332.
11. Loffing J, et al. Altered renal distal tubule structure and renal Na(+) and Ca(2+) handling in a mouse model for Gitelman's syndrome. *J Am Soc Nephrol*. 2004;15(9):2276–2288.
12. Morris RG, Hoorn EJ, Knepper MA. Hypokalemia in a mouse model of Gitelman's syndrome. *Am J Physiol Renal Physiol*. 2006;290(6):F1416–F1420.
13. Soleimani M, et al. Double knockout of pendrin and Na-Cl cotransporter (NCC) causes severe salt wasting, volume depletion, and renal failure. *Proc Natl Acad Sci U S A*. 2012;109(33):13368–13373.
14. Brooks HL, et al. Profiling of renal tubule Na^+ transporter abundances in NHE3 and NCC null mice using targeted proteomics. *J Physiol*. 2001;530(pt 3):359–366.
15. Casselbrant A, et al. Angiotensin II receptors are expressed and functional in human esophageal mucosa. *Am J Physiol Gastrointest Liver Physiol*. 2009;297(5):G1019–G1027.
16. Gagnon KB, Delpire E. Molecular physiology of SPAK and OSR1: two Ste20-related protein kinases regulating ion transport. *Physiol Rev*. 2012;92(4):1577–1617.
17. Welling PA, et al. Multigene kinase network, kidney transport, and salt in essential hypertension. *Kidney Int*. 2010;77(12):1063–1069.
18. van der Lubbe N, et al. Angiotensin II induces phosphorylation of the thiazide-sensitive sodium chloride cotransporter independent of aldosterone. *Kidney Int*. 2011;79(1):66–76.
19. Gonzalez-Villalobos RA, et al. The absence of intrarenal ACE protects against hypertension. *J Clin Invest*. 2013;123(5):2011–2023.
20. Castaneda-Bueno M, et al. Activation of the renal Na^+:Cl^- cotransporter by angiotensin II is a WNK4-dependent process. *Proc Natl Acad Sci U S A*. 2012;109(20):7929–7934.
21. Takahashi D, et al. WNK4 is the major WNK positively regulating NCC in the mouse kidney. *Biosci Rep*. 2014;34(3):e00107.
22. Chiga M, et al. Dietary salt regulates the phosphorylation of OSR1/SPAK kinases and the sodium chloride cotransporter through aldosterone. *Kidney Int*. 2008;74(11):1403–1409.
23. Vallon V, et al. Expression and phosphorylation of the Na^+-Cl^- cotransporter NCC in vivo is regulated by dietary salt, potassium, and SGK1. *Am J Physiol Renal Physiol*. 2009;297(3):F704–F712.
24. van der Lubbe N, et al. Aldosterone does not require angiotensin II to activate NCC through a WNK4-SPAK-dependent pathway. *Pflugers Arch*. 2012;463(6):853–863.
25. Terker AS, et al. Sympathetic stimulation of thiazide-sensitive sodium chloride cotransport in the generation of salt-sensitive hypertension. *Hypertension*. 2014;64(1):178–184.
26. Mu S, et al. Epigenetic modulation of the renal β-adrenergic-WNK4 pathway in salt-sensitive hypertension. *Nat Med*. 2011;17(5):573–580.
27. Richardson C, et al. Activation of the thiazide-sensitive Na^+-Cl^- cotransporter by the WNK-regulated kinases SPAK and OSR1. *J Cell Sci*. 2008;121(pt 5):675–684.
28. Wilson FH, et al. Human hypertension caused by mutations in WNK kinases. *Science*. 2001;293(5532):1107–1112.
29. Yang SS, et al. Molecular pathogenesis of pseudohypoaldosteronism type II: generation and analysis of a Wnk4(D561A/+) knockin mouse model. *Cell Metab*. 2007;5(5):331–344.
30. Lalioti MD, et al. Wnk4 controls blood pressure and potassium homeostasis via regulation of mass and activity of the distal convoluted tubule. *Nat Genet*. 2006;38(10):1124–1132.
31. Wang Y, et al. From the Cover: Whole-genome association study identifies STK39 as a hypertension susceptibility gene. *Proc Natl Acad Sci U S A*. 2009;106(1):226–231.
32. Yang SS, et al. SPAK-knockout mice manifest Gitelman syndrome and impaired vasoconstriction. *J Am Soc Nephrol*. 2010;21(11):1868–1877.
33. Grimm PR, et al. SPAK isoforms and OSR1 regulate sodium-chloride co-transporters in a nephron-specific manner. *J Biol Chem*. 2012;287(45):37673–37690.
34. McCormick JA, et al. A SPAK isoform switch modulates renal salt transport and blood pressure. *Cell Metab*. 2011;14(3):352–364.
35. Huang da W, Sherman BT, Lempicki RA. Systematic and integrative analysis of large gene lists using DAVID bioinformatics resources. *Nat Protoc*. 2009;4(1):44–57.
36. Cheval L, et al. Atlas of gene expression in the mouse kidney: new features of glomerular parietal cells. *Physiol Genomics*. 2011;43(3):161–173.
37. Loffing J, et al. Thiazide treatment of rats provokes apoptosis in distal tubule cells. *Kidney Int*. 1996;50(4):1180–1190.
38. Morsing P, et al. Adaptation of distal convoluted tubule of rats. II. Effects of chronic thiazide infusion. *Am J Physiol*. 1991;261(1 pt 2):F137–F143.
39. Wall SM, et al. Localization of pendrin in mouse kidney. *Am J Physiol Renal Physiol*. 2003;284(1):F229–F241.
40. Kim YH, et al. Immunocytochemical localization of pendrin in intercalated cell subtypes in rat and mouse kidney. *Am J Physiol Renal Physiol*. 2002;283(4):F744–F754.
41. Royaux IE, et al. Pendrin, encoded by the Pendred syndrome gene, resides in the apical region of renal intercalated cells and mediates bicarbonate secretion. *Proc Natl Acad Sci U S A*. 2001;98(7):4221–4226.
42. Vallet M, et al. Pendrin regulation in mouse kidney primarily is chloride-dependent. *J Am Soc Nephrol*. 2006;17(8):2153–2163.
43. Leviel F, et al. The Na^+-dependent chloride-bicarbonate exchanger SLC4A8 mediates an electroneutral Na^+ reabsorption process in the renal cortical collecting ducts of mice. *J Clin Invest*. 2010;120(5):1627–1635.
44. Ercolani L, et al. Colocalization of GAPDH and band 3 (AE1) proteins in rat erythrocytes and kidney intercalated cell membranes. *Am J Physiol*. 1992;262(5 Pt 2):F892–F896.
45. Stehberger PA, et al. Distal renal tubular acidosis in mice lacking the AE1 (band3) Cl^-/$HCO3^-$ exchanger (slc4a1). *J Am Soc Nephrol*. 2007;18(5):1408–1418.
46. Verlander JW, et al. Deoxycorticosterone upregulates PDS (Slc26a4) in mouse kidney: role of pendrin in mineralocorticoid-induced hypertension. *Hypertension*. 2003;42(3):356–362.
47. Verlander JW, et al. Angiotensin II acts through the angiotensin 1a receptor to upregulate pendrin. *Am J Physiol Renal Physiol*. 2011;301(6):F1314–F1325.
48. Verlander JW, et al. Dietary Cl(–) restriction upregulates pendrin expression within the apical plasma membrane of type B intercalated cells. *Am J Phys-*

iol Renal Physiol. 2006;291(4):F833–F839.
49. Azroyan A, et al. Regulation of pendrin by cAMP: possible involvement in β-adrenergic-dependent NaCl retention. *Am J Physiol Renal Physiol*. 2012;302(9):F1180–F1187.
50. Jeong HW, et al. Inactivation of Notch signaling in the renal collecting duct causes nephrogenic diabetes insipidus in mice. *J Clin Invest*. 2009;119(11):3290–3300.
51. Rossier BC. Epithelial sodium channel (ENaC) and the control of blood pressure. *Curr Opin Pharmacol*. 2014;15:33–46.
52. Debonneville C, et al. Phosphorylation of Nedd4-2 by Sgk1 regulates epithelial Na(+) channel cell surface expression. *EMBO J*. 2001;20(24):7052–7709.
53. Wulff P, et al. Impaired renal Na(+) retention in the sgk1-knockout mouse. *J Clin Invest*. 2002;110(9):1263–1268.
54. Hou J, et al. Claudin-4 forms paracellular chloride channel in the kidney and requires claudin-8 for tight junction localization. *Proc Natl Acad Sci U S A*. 2010;107(42):18010–18015.
55. He W, et al. Citric acid cycle intermediates as ligands for orphan G-protein-coupled receptors. *Nature*. 2004;429(6988):188–193.
56. Tokonami N, et al. α-Ketoglutarate regulates acid-base balance through an intrarenal paracrine mechanism. *J Clin Invest*. 2013;123(7):3166–3171.
57. Weiner ID, Verlander JW. Renal ammonia metabolism and transport. *Compr Physiol*. 2013;3(1):201–220.
58. Curthoys NP, Gstraunthaler G. Mechanism of increased renal gene expression during metabolic acidosis. *Am J Physiol Renal Physiol*. 2001;281(3):F381–F390.
59. Abu Hossain S, et al. Cellular and molecular basis of increased ammoniagenesis in potassium deprivation. *Am J Physiol Renal Physiol*. 2011;301(5):F969–F978.
60. McGivan JD, Bungard CI. The transport of glutamine into mammalian cells. *Front Biosci*. 2007;12:874–882.
61. Busque SM, Wagner CA. Potassium restriction, high protein intake, and metabolic acidosis increase expression of the glutamine transporter SNAT3 (Slc38a3) in mouse kidney. *Am J Physiol Renal Physiol*. 2009;297(2):F440–F450.
62. Broer A, et al. Molecular cloning of mouse amino acid transport system B0, a neutral amino acid transporter related to Hartnup disorder. *J Biol Chem*. 2004;279(23):24467–24476.
63. Matsuo H, et al. Identification of a novel Na^+-independent acidic amino acid transporter with structural similarity to the member of a heterodimeric amino acid transporter family associated with unknown heavy chains. *J Biol Chem*. 2002;277(23):21017–21026.
64. Pajor AM. Sodium-coupled dicarboxylate and citrate transporters from the SLC13 family. *Pflugers Arch*. 2014;466(1):119–130.
65. Bahn A, et al. Identification of a new urate and high affinity nicotinate transporter, hOAT10 (SLC22A13). *J Biol Chem*. 2008; 283(24):16332–16341.
66. Lu R, Chan BS, Schuster VL. Cloning of the human kidney PAH transporter: narrow substrate specificity and regulation by protein kinase C. *Am J Physiol*. 1999;276(2 pt 2):F295–F303.
67. Kojima R, et al. Immunolocalization of multispecific organic anion transporters, OAT1, OAT2, and OAT3, in rat kidney. *J Am Soc Nephrol*. 2002;13(4):848–857.
68. Alleyne GA, Scullard GH. Renal metabolic response to acid base changes. I. Enzymatic control of ammoniagenesis in the rat. *J Clin Invest*. 1969;48(2):364–370.
69. Alleyne GA. Concentrations of metabolic intermediates in kidneys of rats with metabolic acidosis. *Nature*. 1968;217(5131):847–848.
70. Wall SM, Weinstein AM. Cortical distal nephron Cl(–) transport in volume homeostasis and blood pressure regulation. *Am J Physiol Renal Physiol*. 2013;305(4):F427–F438.
71. Eladari D, et al. Electroneutral absorption of NaCl by the aldosterone-sensitive distal nephron: implication for normal electrolytes homeostasis and blood pressure regulation. *Cell Mol Life Sci*. 2014;71(15):2879–2895.
72. Jacques T, et al. Overexpression of pendrin in intercalated cells produces chloride-sensitive hypertension. *J Am Soc Nephrol*. 2013;24(7):1104–1113.
73. Chambrey R, et al. Renal intercalated cells are rather energized by a proton than a sodium pump. *Proc Natl Acad Sci U S A*. 2013;110(19):7928–7933.
74. Pela I, Bigozzi M, Bianchi B. Profound hypokalemia and hypochloremic metabolic alkalosis during thiazide therapy in a child with Pendred syndrome. *Clin Nephrol*. 2008;69(6):450–453.
75. Al-Awqati Q. Cell biology of the intercalated cell in the kidney. *FEBS Lett*. 2013;587(13):1911–1914.
76. Gao X, et al. Deletion of hensin/DMBT1 blocks conversion of β- to α-intercalated cells and induces distal renal tubular acidosis. *Proc Natl Acad Sci U S A*. 2010;107(50):21872–21877.
77. Vijayakumar S, et al. Role of integrins in the assembly and function of hensin in intercalated cells. *J Am Soc Nephrol*. 2008;19(6):1079–1091.
78. Fejes-Toth G, Naray-Fejes-Toth A. Differentiation of renal beta-intercalated cells to alpha-intercalated and principal cells in culture. *Proc Natl Acad Sci U S A*. 1992;89(12):5487–5491.
79. Wehrli P, et al. Replication of segment-specific and intercalated cells in the mouse renal collecting system. *Histochem Cell Biol*. 2007;127(4):389–398.
80. Song HK, et al. Origin and fate of pendrin-positive intercalated cells in developing mouse kidney. *J Am Soc Nephrol*. 2007;18(10):2672–2682.
81. Trepiccione F, et al. Evaluation of cellular plasticity in the collecting duct during recovery from lithium-induced nephrogenic diabetes insipidus. *Am J Physiol Renal Physiol*. 2013;305(6):F919–F929.
82. Park EY, et al. Proposed mechanism in the change of cellular composition in the outer medullary collecting duct during potassium homeostasis. *Histol Histopathol*. 2012;27(12):1559–1577.
83. Kim YH, et al. Reduced ENaC protein abundance contributes to the lower blood pressure observed in pendrin-null mice. *Am J Physiol Renal Physiol*. 2007;293(4):F1314–F1324.
84. Pech V, et al. Pendrin modulates ENaC function by changing luminal HCO_3. *J Am Soc Nephrol*. 2010;21(11):1928–1941.
85. Gueutin V, et al. Renal β-intercalated cells maintain body fluid and electrolyte balance. *J Clin Invest*. 2013;123(10):4219–4231.
86. Hadchouel J, et al. Regulation of extracellular fluid volume and blood pressure by pendrin. *Cell Physiol Biochem*. 2011;28(3):505–512.
87. Nissim I, Yudkoff M, Segal S. Metabolic fate of glutamate carbon in rat renal tubules. Studies with 13C nuclear magnetic resonance and gas chromatography-mass spectrometry. *Biochem J*. 1987;241(2):361–370.
88. Kaufhold M, et al. Differential interaction of dicarboxylates with human sodium-dicarboxylate cotransporter 3 and organic anion transporters 1 and 3. *Am J Physiol Renal Physiol*. 2011;301(5):F1026–F1034.
89. Lungkaphin A, Lewchalermwongse B, Chatsudthipong V. Relative contribution of OAT1 and OAT3 transport activities in isolated perfused rabbit renal proximal tubules. *Biochim Biophys Acta*. 2006;1758(6):789–795.
90. Tannen RL, McGill J. Influence of potassium on renal ammonia production. *Am J Physiol*. 1976;231(4):1178–1184.
91. Lee Hamm L, Hering-Smith KS, Nakhoul NL. Acid-base and potassium homeostasis. *Semin Nephrol*. 2013;33(3):257–264.
92. Nagami GT, et al. Effects of acid challenges on type 2 angiotensin II receptor-sensitive ammonia production by the proximal tubule. *Am J Physiol Renal Physiol*. 2014;307(1):F53–F57.
93. Delpire E, Gagnon KB. SPAK and OSR1: STE20 kinases involved in the regulation of ion homoeostasis and volume control in mammalian cells. *Biochem J*. 2008;409(2):321–331.
94. Edgar R, Domrachev M, Lash AE. Gene Expression Omnibus: NCBI gene expression and hybridization array data repository. *Nucleic Acids Res*. 2002;30(1):207–210.
95. Pfaffl MW. A new mathematical model for relative quantification in real-time RT-PCR. *Nucleic Acids Res*. 2001;29(9):e45.
96. Garcia NH, Plato CF, Garvin JL. Fluorescent determination of chloride in nanoliter samples. *Kidney Int*. 1999;55(1):321–325.
97. Wall SM, et al. Contribution of the Na^+-K^+-$2Cl^-$ cotransporter NKCC1 to Cl^- secretion in rat OMCD. *Am J Physiol Renal Physiol*. 2001;280(5):F913–F921.
98. Wall SM, et al. NaCl restriction upregulates renal Slc26a4 through subcellular redistribution: role in Cl^- conservation. *Hypertension*. 2004;44(6):982–987.
99. Knepper MA, Good DW, Burg MB. Mechanism of ammonia secretion by cortical collecting ducts of rabbits. *Am J Physiol*. 1984;247(5 pt 2):F729–F738.
100. Knepper MA, Good DW, Burg MB. Ammonia and bicarbonate transport by rat cortical collecting ducts perfused in vitro. *Am J Physiol*. 1985; 249(6 pt 2):F870–F877.
101. Merz WA. Die Strecken messung an gerichteten Struktwuren in Mikroskop und ihre Anwedung zur Bestimmung von Oberflachen-Volumen-Relationen im Knochengewebe. *Mikroskopie*. 1967;22(5):132–142.